Spectroscopic analysis of hot subluminous stars from the Hamburg Quasar Survey: New atmospheric- and stellar parameters

Bachelorarbeit aus der Physik

Vorgelegt von

Lennard Kufleitner

10.04.2024

Revised: 10.06.2024

Dr. Karl Remeis-Sternwarte Bamberg
Friedrich-Alexander-Universität Erlangen-Nürnberg

Betreuer: Prof. Dr. Ulrich Heber

Abstract

The binary evolution of stars is an interesting field of study in stellar astrophysics. Hot subdwarfs are a class of stars that are very useful for this research as they do not form via the fairly well understood single-star evolution but through interacting binary evolution. In this thesis I perform an analysis of a sample of hot subdwarfs of spectral types sdB and sdOB from the spectroscopic follow-up to the Hamburg Quasar Survey which were discovered by Edelmann et al. (2003). By performing a spectroscopic analysis of the spectra obtained during the follow-up new atmospheric parameters are derived with a new grid of model spectra and a global fitting method both different from the previous study by Edelmann et al. (2003). The comparison between the atmospheric parameters presented in Edelmann et al. (2003) and the parameters found in this analysis shows a trend in the derived temperatures which could be explained by the new model grids used where here one hybrid LTE/NLTE model grid is used whereas in Edelmann et al. (2003) three different grids are used depending on the temperature of the star. Independent spectra were taken from the SDSS/LAMOST surveys and spectroscopically analyzed which showed no systematic differences to the spectra from the HQS follow-up. Then a photometric fit is performed by using the data from many photometric surveys to derive the stellar parameters radius, luminosity and mass for this sample for the first time by combining the information obtained from the spectroscopy and photometry with the parallaxes measured by the Gaia satellite. Composite subdwarf systems found spectroscopically by Edelmann et al. (2003) are confirmed by the SED analysis. In addition three star systems of the sample which were not classified as composite in Edelmann et al. (2003) are shown to be composite here. Furthermore, the stellar parameters which were derived for the non-composite stars are found to be in agreement with predictions by canonical evolution models with a median of the mass distribution of 0.433 $M_{\odot}$, radii in the range of 0.1 to 0.3 $R_{\odot}$ and luminosities in the range of 10 to 30 $L_{\odot}$. Additionally the stellar parameters radius and luminosity for the composite hot subdwarfs show a similar radius/luminosity-temperature distribution to the non-composite subdwarfs. The companions to the non-composite subdwarfs show stellar parameters consistent with main-sequence stars. The HQS sample forms a reference sample for large spectroscopic surveys like 4MOST to come.

Contents

List of Figures

List of Tables

1. Introduction

The mission of stellar astrophysics is to investigate the properties and behaviour of stars and to develop an understanding of how they work. One part of this field is stellar evolution which studies what happens in and around stars throughout their lifetime from birth to death and beyond. The inner workings of the stellar evolution of single stars is fairly well understood up to this point. However what became an interesting object of study in the last decades is the effects of binary evolution of stars and how stars can interact with each other in different stages of their lifetimes. When studying binary evolution one class of stars provide a particularly interesting playing ground as they are believed to be produced by binary evolution: The hot subdwarfs. In this thesis we will take a look at the spectra of the follow-up to the Hamburg Quasar Survey by Edelmann et al. (2003) and combine them with information gained by photometric data and parallaxes from the Gaia mission to obtain stellar parameters for a sample of 111 stars to compare with predictions from theoretical predictions.

1.1. Hot subdwarfs

Hot subdwarfs are quite different from the "normal" subdwarfs with whom they share their name. Normal subdwarfs are just core hydrogen-burning stars with a particularly low metallicity which offsets them from the main-sequence stars and can be seen around the F to K spectral types in the Hertzsprung-Russell diagram (HRD) that is drawn in Figure 1. The hot subdwarfs can be found in the region that is denoted by `EHB` in Figure 1 which stands for Extreme Horizontal Branch.

1.1.1. Properties

The properties of hot subdwarfs further differ from "normal" subdwarfs by the fact that they are core-helium burning stars that reside at the blue end of the horizontal branch (Heber (2009)). They can further be classified into different groups depending on the features of their spectra (see Heber (2009)).

- **sdB stars**: sdBs are hot subdwarfs with temperatures/colours that are in the range of main-sequence B stars but are less luminous than them. Furthermore they are characterized by having broader Balmer absorption lines in their spectra than main-sequence B-stars. Additionally sdBs often show relatively weak HeI absorption lines in their spectra.
- **sdOB stars**: sdOB stars form a middle ground between sdBs and sdOs.

Their spectra are similar to sdBs but they also show weak HeII (single-ionized Helium) absorption lines.

- **sdO stars**: sdOs are hotter than sdBs with temperatures in the range of main-sequence O stars. They show the HeII line at 4686 Å and are often relatively helium rich. In some cases they do not show hydrogen Balmer lines.

To understand the origin of hot sudwarfs let's first take a look at the evolution of single stars with low masses $M < 8\,\mathrm{M}_\odot$.

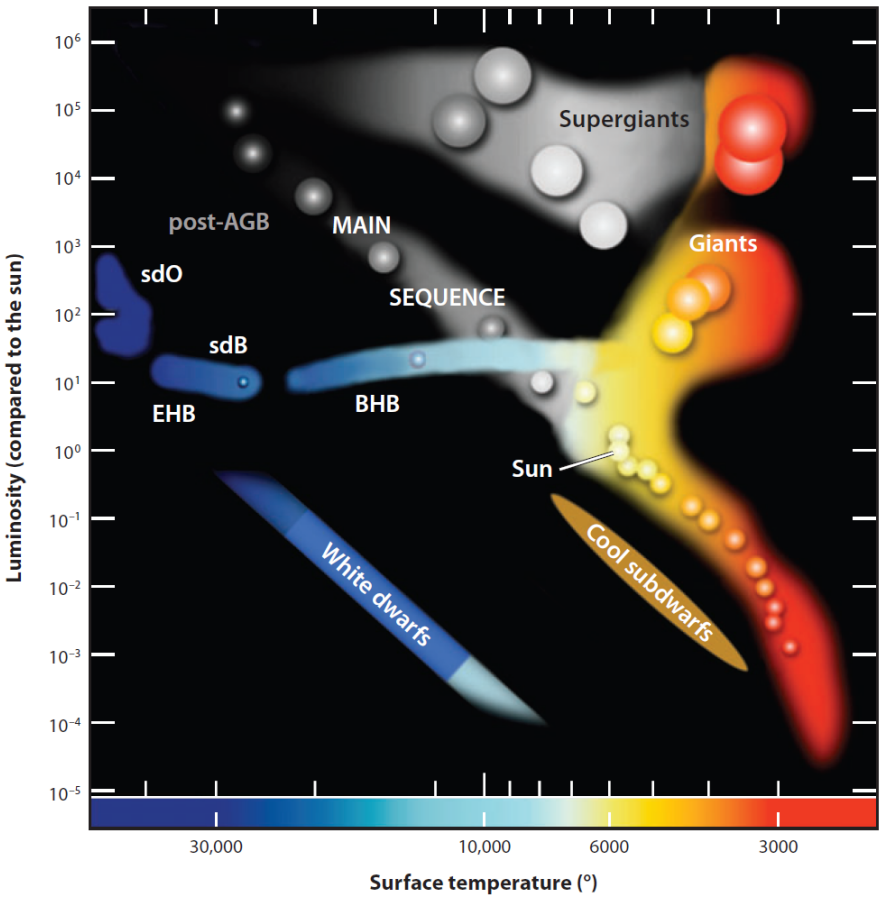

Figure 1: This sketch shows a Hertzsprung-Russell diagram which is a plot of the luminosity of a star against the the surface temperature of the star. The hot subdwarfs can be seen in the region with the name EHB. Taken from Heber (2009).

1.1.2. Evolution of single low mass stars

In the single-star evolution a star starts its journey on the main-sequence in the HRD (see Figure 1) with a particular mass that is determined by the available material in its region during its formation. It remains on this main-sequence for most of its life by generating energy in its core by hydrogen fusion which counteracts the gravitational force that is trying to collapse it. Once the hydrogen in its core runs low and the core consists of helium temperatures rise in the shell around the core which stars hydrogen fusion in the shell. This leads to an expansion of the star and the star leaves the main-sequence in the HRD to become a red giant that belongs to the red giant branch (RGB) (denoted by `Giants` in Figure 1). At the tip of the RGB if the star had a initial mass of (1.8 to 2.2 $M_{\odot}$, see Padmanabhan (2000)) the violent helium flash takes place when helium fusion stars in the core. After the helium flash the now core-helium burning star belongs to the horizontal branch (HB) which is shown as the whole horizontal bar denoted by `BHB` in Figure 1 where the BHB is the blue part of the HB. Once helium runs out in the core of the HB star hydrogen and helium fusion now take place in the shell of the stars which expands the star and leads it to once again become a giant that belongs to the asymptotic giant branch (AGB). At the tip of the AGB the envolope of the star is ejected as a planetary nebula and what remains is the carbon/oxygen core of the star as a white dwarf that is held up by the degeneracy pressure of its electrons.

1.1.3. Binary evolution of hot subdwarfs

As many sdB stars are found in binary systems and mass loss during the RGB phase is required to form hot subdwarfs (see Heber (2009)) stellar evolution in binary systems is important for the formation of hot subdwarfs. There are three generally reasonable channels for their formation which were identified by Han et al. (2003).

- **Common Envelope (CE)**: Here the progenitor of the sdB star which is a giant that belongs to the RGB is near the tip of the RGB and fills its Roche lobe which causes unstable Roche lobe overflow from the RGB star to its companion which requires a mass ratio of $q > 1.2 - 1.5$. As the companion can not hold this material a CE forms around the binary system in which drag due to the CE causes the system to become a close-binary with periods in the range of 0.1 to 10 days. This scenario can be seen in part b) of Figure 2 where the results is a sdB-main-sequence-star binary and in part a) where the binary partner to the progenitor of the sdB star has become a white dwarf and transferred some of its mass to the sdB-progenitor

by stable Roche lobe overflow where the results is a sdB-white-dwarf binary (see Heber (2009)).

- **Stable Roche lobe overflow (SRLOF)**: If the mass ratio between the sdB-progenitors and its companion is below 1.2-1.5 stable Roche lobe overflow can occur between them when the sdB-progenitor is near the tip of the RGB. This leaves behind a wide binary with periods of 10 - 500 days (see Heber (2009)).
- **White Dwarf Merger**: The existence of single sdB and sdO stars could be explained by the merging of a close white dwarf- white dwarf binary. This merger is made possible by the emission of gravitational waves which causes the shrinking of the orbit until the stars finally merge (see Heber (2009)).

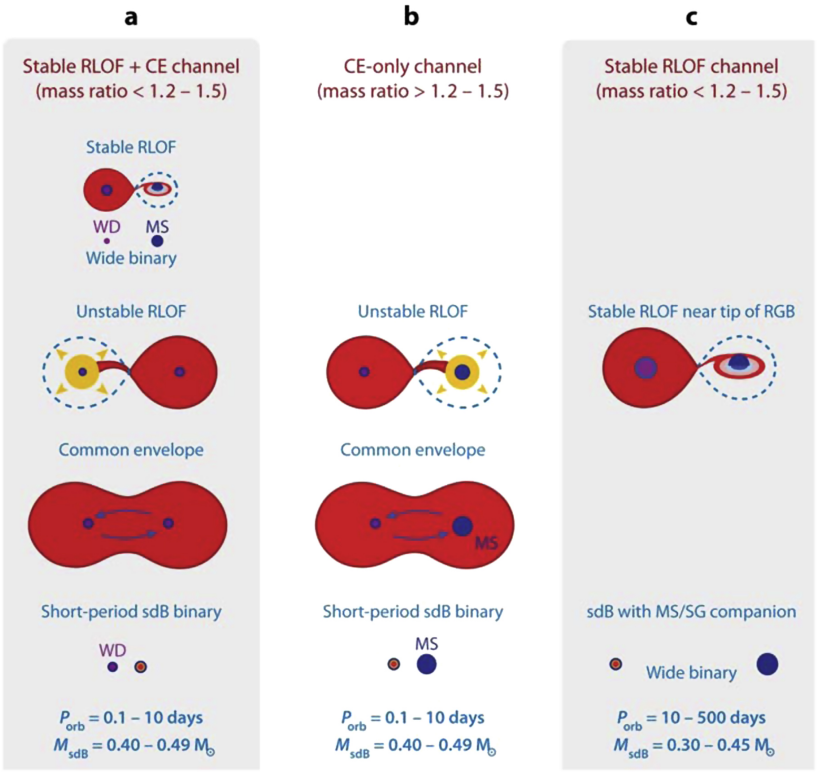

Figure 2: Three different formation scenarios for sdB stars. Part a) describes a formation channel for stars with mass ratios below 1.2-1.5 with stable Roche lobe overflow for the more massive star and . Part b) shows the common envelope scenario for a mass ratio of greater than 1.2 to 1.5. Part c) shows an alternative stable Roche lobe overflow channel for the formation of wide binaries. Taken from Heber (2016a).

1.2. Hamburg Quasar Survey-Spectroscopic follow-up

The spectra for the sample of stars used in this thesis come from the spectroscopic follow-up to the Hamburg Quasar Survey (HQS). The HQS survey (Hagen et al., 1995) was a wide-angle objective prism survey for the northern sky performed with the 80 cm Schmidt telescope at the German-Spanish Astronomical Center (DSAZ) on Calar Alto, Spain. It began in 1980 and by 1993 it covered an area of 11 000 deg^2. Its main goal was to create a sample of bright quasars but it also was a rich source of faint blue stars with magnitudes in the range of $13.5 < B < 18.5$. The objective prism spectra had a resolution of 45 Å at H_γ and from these spectra hot star candidates were selected by a collaboration of the institutes from Hamburg, Kiel, Tübingen and Bamberg to obtain higher resolution spectra and identify hot subdwarfs. In the sample used in this thesis the focus was on sdB stars and all spectra used come from Edelmann et al. (2003).

In Figure 3 I show the positions of the sample of stars in the Galaxy from Edelmann et al. (2003). Most stars are above or below the disk of the Milky Way.

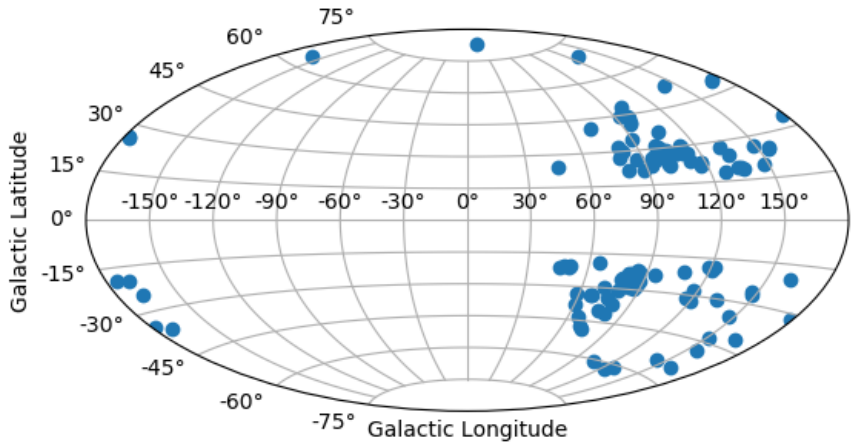

Figure 3: Positions of the sample of stars in Galactic coordinates in the Aitoff projection.

The spectroscopic follow-up consisted of several observing runs from 1989 to 1998 with different instruments at the DSAZ on Calar Alto, Spain. The telescopes that were used were the 3.5m telescope for most of the observations and the 2.2m telescope. Information about the oberving runs is shown in Table 1 of Edelmann et al. (2003). The spectrographs used are the following:

- **TWIN**: The TWIN spectrograph was attached to the 3.5m telescope. The light from the telescope first goes through a slit and was then split into two parts by a dichroic mirror: the blue part optimized for the range of 3200 Å to 5500 Å and the red part optimized for the range of 5000 Å to 10 000 Å. A grating then splits the light into its wavelength components for each channel and a CCD records an image of the spectrum. With this spectrograph intermediate resolution spectra can be taken with resolving powers of $R = 3000$ to $R = 14000$ (see Graser (1998)).

- **B&C**: A Boller & Chivens (B&C) spectrograph was attached to the 3.5m telescope. In its observing run it only covered the spectral range from 3850 Å to 5650 Å with an intermediate resolution of 5 Å.

- **FR**: The Focal Reducer (FR) spectrograph was mounted to the 3.5m telescope. FR was used in one observing run from 1990-09-01 to 1990-10-09 where it covered the spectral range from 3770 Å to 5550 Å with an intermediate resolution of 7 Å.

- **CAS**: The CAS spectrograph was attached to the 2.2 meter telescope. During its run the effects due to the seeing were sometimes smaller than the slit which lead to a varying of the spectral resolution between 4.5 Å and 5.5 Å in the covered spectral range from 4010 Å to 6720 Å.

- **CAFOS**:The Calar Alto Faint Object Spectrograph (CAFOS) was mounted to the 2.2m telescope and its light-splitting apparatus is a grism which combines a grating and a prism. Here the seeing also varied during the run leading to resolutions between 5 Å and 8 Å with a spectral range from 3400 Å to 6300 Å.

1.3. Photometric surveys

Beyond the spectroscopy from which one gains the atmospheric parameters photometry is needed to determine stellar parameters. This photometric data is obtained from photometric surveys which range from the UV to the Infrared. A full list of the photometric surveys used in this thesis can be found in Culpan et al. (2024).

One survey that is particularly important, however, is the GALEX survey. The Galaxy Evolution Explorer (GALEX) is a space-satellite that performed an all-sky survey in the UV from 2003 to 2013 (Martin et al., 2005). It does this in two photometric bands one with a spectral range from 1350 Å to 1750 Å, the FUV band and one with a spectral range from 1750 Å to 2750 Å, the NUV band. It is important as its coverage of the UV helps constrain the interstellar reddening of the interstellar medium as this extinction is strongest at lower wavelengths (Fitzpatrick, 1999). Before the wide coverage of the spectrum by many different surveys from the UV to the Infrared the interstellar reddening of stellar populations could be estimated by plotting the apparent magnitude of a population of stars like the Johnson V-Band against a colour index like the Johnson B-V index and fitting an isochrone to match the data (Ashman and Zepf, 2008). With the photometric surveys covering a wide range of wavelengths and photometric fitting the interstellar reddening can be constrained on individual stars as is shown in section 2.2.

1.4. Gaia and annual parallaxes

The key to determine the stellar parameters of stars is in knowing their distance. A direct way of measuring the distance is through the annual parallax. The trigonometric parallax is due to the apparent motion of nearby stars compared to further away background star as the Earth travels around the Sun. The parallax p (or later $\overline{\omega}$) is the angle that is made by the star when observing it over a 6 month period for example in January and in July as can be seen in Figure 4. With trigonometry and the small angle approximation the parallax is then:

$$p = \frac{1 \text{ AU}}{d} \ , \tag{1}$$

where d is the distance in parsecs which is the distance a star has when the parallax is 1 mas and the astronomical unit 1 AU $\approx 150 \times 10^9$ m is the distance between the Earth and the Sun.

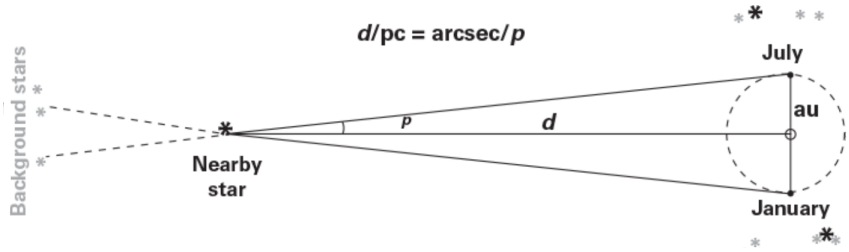

Figure 4: This sketch illustrates the definition of the parallax p of the nearby star as the Earth goes around the sun. Taken from Owocki (2021).

One important goal of the Gaia mission is to measure these parallaxes with high precision that has not been achieved in previous missions like the Hipparcos mission to which it is the successor. The Gaia space mission (Prusti et al., 2016) is a mission of the European Space Agency (ESA) which was launched to space on 19.12.2013. An illustration of the Gaia satellite can be seen in Figure 5. The current data release 3 (DR3) contains the astrometric parameters position, proper motion and parallax for 1.5 billion sources. The positions and parallaxes for the stars of this thesis are taken from this data release.

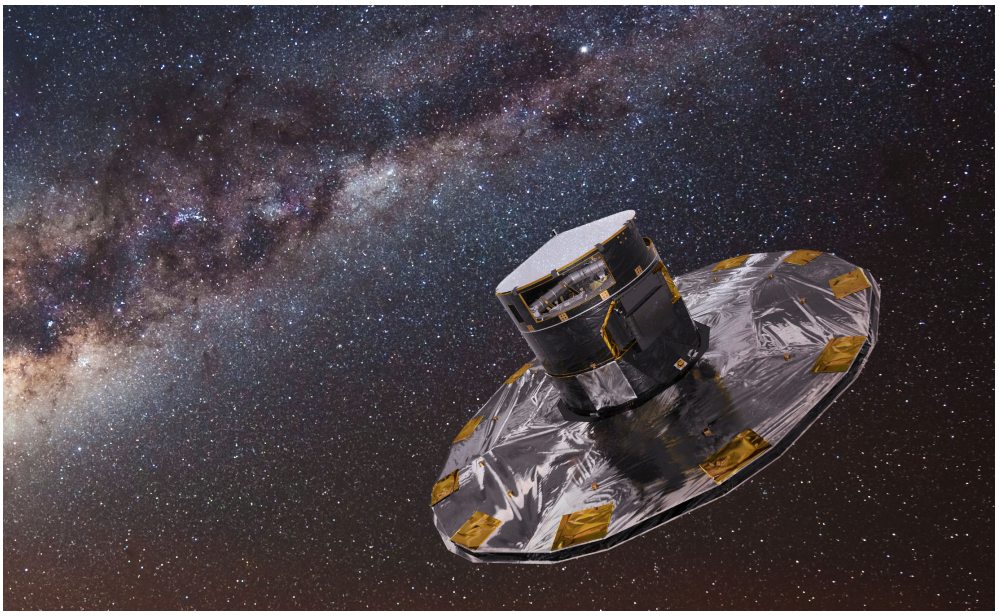

Figure 5: Illustration of the Gaia satellite. Taken from ESA (2013).

2. Methods

The goal is to determine the atmospheric and stellar parameters of the hot subdwarfs in the Hamburg Quasar Survey sample. The three tools necessary for this are spectral analysis of optical spectra taken during the spectroscopic follow-up to the HQS survey, analysis of photometric measurements of several stellar surveys which have been performed during the last few decades and the trigonometric parallaxes, which recently became available due to the Gaia mission.

2.1. Spectral Analysis

To begin with the analysis one has to take a look at the spectra which are used to determine the atmospheric parameters like effective temperature T_{eff}, surface gravity $\log g$ and helium abundance $\log \text{He}$. But first what are astronomical spectra?

A spectrum is the intensity of light as a function of its wavelength. By analysing this wavelength dependence one can get clues about the mechanisms that caused this specific wavelength dependence and therefore the properties of the star that emitted this light.

2.1.1. Model Photospheres

At the heart of the attempt to determine atmospheric parameters from spectra is the theoretical model that is used to fit to the observation. For this one needs a way to calculate the emergent flux that is emitted by a star. The following is based on Crivellari, Simón-Díaz, and Arévalo (2020) and Gray (2021). The specific intensity of the radiation field $I(r, t, \vec{\mathbf{n}})$ at position r, time t in direction $\vec{\mathbf{n}}$ is defined as:

$$I(r, t, \vec{\mathbf{n}}) = \frac{\mathrm{d}E_\nu}{\mathrm{d}S \cos\theta \, \mathrm{d}\Omega \, \mathrm{d}t \, \mathrm{d}\nu} \ , \tag{2}$$

where E_ν is the energy of the light with frequencies between ν and $\nu + \mathrm{d}\nu$, $\mathrm{d}S$ is the area crossed by the light, $\mathrm{d}\Omega = \sin\theta \, \mathrm{d}\theta \, \mathrm{d}\varphi$ is the solid angle with polar angle θ and azimuthal angle φ which is determined by the direction $\vec{\mathbf{n}}$ and $\mathrm{d}t$ is the time passed. The specific intensity itself is a scalar function and the direction is seen as a parameter. The units of the specific intensity are $erg\ cm^{-2}\ s^{-1}\ Hz^{-1}\ str^{-1}$.

After light is emitted at the core of the star it has to travel through the star where it will interact with the medium. How light interacts is described by the Radiative Transfer Equation (RTE) which is a differential equation for the specific

intensity and in its general form reads:

$$\frac{\partial I(r,t,\vec{\mathbf{n}})/c}{\partial t} + \boldsymbol{\nabla} \cdot (I(r,t,\vec{\mathbf{n}}) \cdot n) = \eta(r) - \chi(r) J(r,t) \quad , \tag{3}$$

where $\eta(r)$ is the emission coefficient, $\chi(r)$ is the extinction coefficient and $J(r,t) = \frac{1}{4\pi} \oint I(r,t,\vec{\mathbf{n}})\, \mathrm{d}\Omega$ is the mean intensity.

The emission and extinction coefficient are lastly what describes the physical processes inside the star by which the light interacts. The extinction coefficient is also in relation to the specific intensity by the differential equation:

$$\frac{\mathrm{d}I(r,t,\vec{\mathbf{n}})}{\mathrm{d}s} = -\chi(r) I(r,t,\vec{\mathbf{n}}) \ , \tag{4}$$

where $\mathrm{d}s$ is the path length along the direction vector $\vec{\mathbf{n}}$.

In order to make the RTE solvable a few approximations are made in the model atmospheres used in this work.

Time-Independence:
The RTE simplifies under the assumption of time-independence which means that the quantities that describe the radiation in the star, i.e. the specific intensity, emission and extinction coefficients are assumed to not vary with time. With this assumption effects like flares or sunspots are ignored. The RTE then reads:

$$\boldsymbol{\nabla} \cdot (I(r,\vec{\mathbf{n}}) \cdot n) = \eta(r) - \chi(r) J(r) \ , \tag{5}$$

where now the time derivative vanishes.

Plane-parallel geometry:
The complexity of the RTE can be reduced further by introducing a plane-parallel geometry. Here the stellar photosphere is divided up into layers where each of these layers is homogeneous which means that the properties of the radiation field are the same in each layer and only change along one, the radial, direction. This means the derivatives along two of the coordinate axes vanish and only one remains non-zero which is here chosen to be the z-axis. Under the assumption of time-independence and plane-parallel geometry the RTE then reads:

$$\mu \frac{\mathrm{d}I(z,\mu)}{\mathrm{d}z} = \eta(z) - \chi(z) I(z,\mu) \ , \tag{6}$$

where $\mu = \vec{(}e_z) \cdot \vec{\mathbf{n}} = \cos\theta$ which means that θ is the angle between the plane and the direction of the light.
The assumption of a plane-parallel geometry holds when the photosphere is small

in comparison to the total stellar radius.

The radiative flux F_ν that leaves the star for a plane-parallel geometry is then:

$$F_\nu(R) = 2\pi \int_0^1 I(R,\mu) \cdot \mu \, \mathrm{d}\mu \tag{7}$$

The RTE can be rewritten in terms of the source function $S = \frac{\eta}{\chi}$ which is defined by the emission and extinction coefficients which are determined by the physical mechanisms at play:

$$\mu \frac{\mathrm{d}I(z,\mu)}{\mathrm{d}z} = I(z,\mu) - S(z) \ . \tag{8}$$

The emergent specific intensity at the surface is then:

$$I(\tau = 0, \mu) = \int_{\tau=0}^{\tau=\infty} S(t) \exp(-t/\mu) \frac{\mathrm{d}t}{\mu} \ , \tag{9}$$

where the τ is the optical depth defined by the differential equation $\mathrm{d}\tau = -\chi \, \mathrm{d}s$. If the whole photosphere were in thermodynamical equilibrium (TE) the source function would simply be the Planck distribution at the temperature T:

$$S = B(T) = \frac{2h\nu^3}{c^3} \frac{1}{\exp\left(\frac{h\nu}{k_\mathrm{B}T}\right) - 1} \ . \tag{10}$$

Local Thermodynamic Equlibrium However the temperature changes within the star which leads to another approximation to solve the RTE. In local thermodynamical equilibrium (LTE) we assume that every point in the photosphere is in TE with its own, now position-dependent, temperature T. The source function consists then of the Planck distribution for each point.

$$S(\tau) = B(T(\tau)) \tag{11}$$

This approximation is valid as long as the radiation field is bound to small regions when for example collision rates are high which means that the mean free path length becomes small. Under the assumption of LTE the temperature can be determined by looking at three equations.

Maxwell-Boltzmann distribution

In LTE the particles follow the Maxwell-Boltzmann velocity distribution which says:

$$f(v) \, \mathrm{d}v = \frac{\mathrm{d}N(v)}{N_\mathrm{tot}} = \left(\frac{m}{2\pi k_\mathrm{B} T}\right)^{3/2} 4\pi v^2 \exp\left(-mv^2/(2k_\mathrm{B}T)\right) \mathrm{d}v \ , \tag{12}$$

where N_{tot} is the number of particles and T is the local temperature.

Saha ionization equation

When considering that the atoms of different species can have differently populated degrees of ionisation the Saha ionization equation becomes useful. It gives the number of particles of a atomic species N_i in ionization degree i compared to number in ionization degree $i+1$:

$$\frac{N_i}{N_{i+1}} = \left(\frac{h^2}{2\pi m_e k_{\mathrm{B}}}\right) N_e \frac{U_i}{U_{i+1}} T^{-3/2} \exp(\chi_i/(k_{\mathrm{B}}T)) \ , \tag{13}$$

where N_e is the particle density of the electrons, $U = \sum_i g_i \exp(-\chi_i/(k_{\mathrm{B}}T))$ are the partition functions with the statistical weights g_i and χ_i is the ionization energy.

Boltzmann excitation equation

The population of atoms can vary not only in the degree of ionization but also with electrons in different energy levels. The Boltzmann excitation equation describes how two energy levels n_i and n_j with the same degree of ionization compare to each other and reads:

$$\frac{n_i}{n_j} = \frac{g_i}{g_j} \exp(-(E_i - E_j)/(k_{\mathrm{B}}T)) \ , \tag{14}$$

where E_i and E_j are the energies of the two different levels i and j and $g_i = 2J+1$ is the statistical weight of level i with the quantum number J.

Non-LTE

When all these equations are in equilibrium the LTE approximation is valid. For hotter stars however there are departures from these equilibria as the mean free path length gets bigger and there is no local thermodynamic equilibrium anymore. These Non-LTE (NLTE) effects are then computed by using the statistical equilibrium equation.

With the statistical equilibrium equation one can calculate the population of energy levels of atoms. It reads:

$$\sum_{j \neq i} n_i P_{ij} = \sum_{j \neq i} n_j P_{ji} \ , \tag{15}$$

where n_i and n_j are the population densities of energy levels i and j, P_{ij} is the rate of transitions from energy level i to any other level j and P_{ji} is the rate of transitions that increase the population of the energy level i. The rate of processes is usually divided into two components $P_{ij} = R_{ij} + C_{ij}$ and $P_{ji} = R_{ji} + C_{ji}$. The processes denoted by R are radiative processes and the ones denoted by C are collisional processes that do not depend on the radiation field.

Because the statistical equilibrium equation depends on the radiation field and the radiation field depends on the source function through the RTE which depends on the population of the energy levels, the equations that are to be solved are coupled.

The approach for the model grid used for the hot subdwarfs in this work is a hybrid LTE/Non-LTE method which is described in Irrgang, Kreuzer, et al. (2018). Here the first step is to calculate a LTE model with the `ATLAS12` code (Kurucz, 1996). The NLTE effects are then considered by solving for the atomic populations with the `Detail` code (Giddings, 1981). Lastly the final spectrum is calculated with the `Surface` code (Giddings, 1981).

The models which are then used for the fitting process for the sdB/sdOB stars consists of a grid with possible temperatures in the range of $15\,000\,\mathrm{K} < T_{\mathrm{eff}} < 55\,000\,\mathrm{K}$ in steps of 1000 K, surface gravities in the range of $4.6 < \log g < 6.6$ in steps of 0.2 dex and helium abundances in the range of $-5.05 < \log \mathrm{He} < -0.041$ in steps of 0.5 dex except near the maximum value where there are three models with $\log \mathrm{He} = -0.3, \log \mathrm{He} = -0.125$ and $\log \mathrm{He} = -0.041$. This model grid was computed by U. Heber.

Beyond the model spectra of the stars another model grid was used in addition to the stellar spectrum for telluric features in the spectrum, i.e. those features produced by the earths atmosphere. These models were taken from Moehler et al. (2014).

2.1.2. Fitting Procedure

With the model grid of photosphere spectra one can now fit them to the observed spectra. The fitting method that is used in this work was produced by Irrgang, Przybilla, et al. (2014) and is written using the Interactive Spectral Interpretation System by Houck and Denicola (2000).

The procedure is based on the χ^2-minimization method and works by comparing the model spectra from the grid to the observed data and minimizing the statistical χ^2-quantity. This quantity is defined by:

$$\chi^2 = \sum_i \chi_i^2 = \sum_i \left(\frac{f_i - f_{\mathrm{model},i}}{\delta_i} \right)^2 \quad , \tag{16}$$

where f_i is the observed flux, $f_{\mathrm{model},i}$ is the flux from the model spectra and δ_i

is the uncertainty of the observed flux and i indicates each data point. During the minimization process the reduced χ^2 which is χ^2/f where f are the degrees of freedom which are calculated by subtracting the number of free fit parameters from the number of data points is brought closer to its optimal value at reduced $\chi^2 = 1$. When the reduced χ^2 goes below one this could mean that the the measurement uncertainties were overestimated. The measurement uncertainties δ_i can be estimated by assuming that the noise on each data point follows a Gaussian distribution.

During the fitting process the first step is to consider the resolution limitation of the used spectrograph. To do this a convolution between the observed spectrum and a Gaussian profile with a full width at half maximum of $\Delta\lambda = \lambda/R$ where R is the resolving power is performed. The resolution for each star spectrum $\Delta\lambda$ is given in Table 1 of appendix A.

Afterwards one needs to normalize the spectrum. This is done by choosing suitable points in the spectrum and fitting a cubic spline to the continuum. In the next step the cubic spline is fitted along with the radial velocity shift. This radial velocity shift is primarily caused by the Doppler effect where the light from a star that is moving away from us is redshifted and a star that is moving towards us is blueshifted. This causes a shift in the spectrum which can be measured from the spectral absorption lines The amount of this shift in the wavelength is:

$$\frac{v_{\mathrm{rad}}}{c} = \frac{\Delta\lambda}{\lambda} \ , \tag{17}$$

where v_{rad} is the radial velocity of the star and $\Delta\lambda$ is the shift in wavelength. Then in the next step after the spectrum is normalized by dividing the observed spectra by the cubic spline fit the parameters of the model spectra are fitted to the observed spectrum. To do this the values in the model grid are linearly interpolated between the grid members. The important resulting parameters are then the effective temperature T_{eff}, the surface gravity $\log g$ and the helium abundance $\log \mathrm{He}$.

The uncertainties on these parameters are gained by varying the specific parameter and fitting all other parameters until χ^2 reaches a certain level which has a difference to the minimum of $\Delta\chi^2$. Here we use a $\Delta\chi^2 = 1$ which corresponds to 1σ errors. The uncertainties are furthermore of statistical nature and do not include systematic uncertainties which could be caused by inaccuracies in the model spectra or in the instrumental apparatus. For this reason the uncertainties on the

temperature is modified by

$$\sigma_{\mathrm{T}} = \sqrt{\sigma^2_{\mathrm{T,stat}} + (3\% \cdot T)^2} \tag{18}$$

and the surface gravity uncertainties are modified by

$$\sigma_{\log g} = \sqrt{\sigma^2_{\log g,\mathrm{stat}} + 0.1^2}\ . \tag{19}$$

2.2. Photometric and Astrometric Analysis

To analyze the stars in this sample further spectral energy distribution (SED) fits are performed. One goal of this is to detect whether the observed system is a composite system or apparently single and to gain the stellar parameters mass, radius and luminosity.

A SED fit is the fit of a model spectrum to a collection of broad-band photometric measurements. These photometric measurements come from several photometric surveys and are the data that is to be fitted to the models. For each SED fit there are two components, one for the hot subdwarf star and one for the potential composite partner star.

2.2.1. Spectral Energy Distributions

The model grids from which the theoretical SED are synthesized depend on which of the two components of the SED are considered. For the sdB/sdOB stars the same model grid is used as for the spectrosopic fits. For the composite cooler partner a different grid is used by Husser et al. (2013). This grid contains model spectra for temperatures in the range of $2300\,\mathrm{K} < T < 7000\,\mathrm{K}$ with a step size of 100 K and surface gravities in the range of $2 < \log g < 5.5$ with a step size of 0.5 dex which allows for the detection of cool companion stars.

2.2.2. Fitting Procedure

The fitting method that is used was developed by Heber, Irrgang, and J. Schaffenroth (2018). The first step in this procedure is to automatically gather the photometric data which is done by using the Table Access Protocoll (TAP) and the VizieR database for the star by using its coordinates from the Gaia mission. Here unusable data which have error flags can be filtered out as well.

To compare the observational magnitudes to the model spectra one has to first calculate synthetic magnitudes from these spectra. This can be done by passing

our model spectra through the pass-band of the instrumental response function for the specific filter from a survey. The apparent magnitude mag_x for a photometric filter x is:

$$\mathrm{mag}_x = -2.5 \log \left(\frac{\int_0^\infty r_x(\lambda) f(\lambda) \lambda \, \mathrm{d}\lambda}{\int_0^\infty r_x(\lambda) f^{\mathrm{ref}}(\lambda) \lambda \, \mathrm{d}\lambda} \right) + \mathrm{mag}_x^{\mathrm{ref}} \, , \tag{20}$$

where $r_x(\lambda)$ is the instrumental response function, $f(\lambda)$ is the flux that arrives at the detector and $f^{\mathrm{ref}}(\lambda)$,$\mathrm{mag}_x^{\mathrm{ref}}$ are the flux and magnitude that belong to a reference star which is Vega such that the zero-point of the magnitude scale can be set.

The flux from the star that arrives at the detector $f(\lambda)$ can be rewritten in terms of the flux that originated from the stars surface $F(\lambda)$ which s also flux from the model spectra. This is done by using the relation:

$$f(\lambda) = \frac{\Theta^2 F(\lambda)}{4} \, , \tag{21}$$

where $\Theta = 2R/d$ is the angular diameter of the star with radius R and distance d.

An extra effect that needs to be considered in the calculation of synthetic magnitudes is the interstellar absorption by the interstellar medium. This is done by introducing the wavelength-dependent total extinction $A(\lambda)$ (Fitzpatrick et al., 2019) which is given by

$$A(\lambda) = -2.5 \log \frac{f(\lambda)}{F(\lambda)} + 5 \log \Theta/2 \, . \tag{22}$$

This gives the synthetic magnitudes:

$$\mathrm{mag}_x = -2.5 \log \left(\frac{\Theta^2 \int_0^\infty r_x(\lambda) 10^{(-0.4 A(\lambda))} F(\lambda) \lambda \, \mathrm{d}\lambda}{\int_0^\infty r_x(\lambda) f^{\mathrm{ref}}(\lambda) \lambda \, \mathrm{d}\lambda} \right) + \mathrm{mag}_x^{\mathrm{ref}} \, , \tag{23}$$

The total extinction $A(\lambda)$ is related to the colour excess $E(44-55)$ and the extinction parameter $R(55)$ by

$$R(55) = \frac{A(55)}{E(44-55)} \, , \tag{24}$$

where 44 and 55 stand for the wavelengths 4400 Å and 5500 Å. The parameter $R(55)$ is fixed to the value 3.02 during the fit as this is the mean value for absorption in the Milky Way which means that the strength of the interstellar absorption is controlled by the colour excess $E(44-55)$.

The spectra of the two stars, the hot subdwarf and the cooler companion are fitted simultaneously by introducing the surface ratio S and angular diameter $\Theta_{\rm cool}$ which blends between the two model spectra. The parameters that are fitted for the SEDs are the angular diameters Θ and $\Theta_{\rm cool}$, the colour excess $E(44-55)$ and the surface ratio S. The temperatures, surface gravities and helium abundances come from the spectroscopic fit.

2.2.3. Parallax and Stellar Parameters

The stellar parameters mass, radius and luminosity can be calculated by using the parameters which were derived from the spectral and photometric analysis and combining them with the parallaxes from the Gaia mission.

First the parallax $\overline{\omega}$ can be used in the calculation of the radius:

$$R = \frac{\Theta}{2\overline{\omega}} \ . \tag{25}$$

This results in being able to calculate the luminosity of the star:

$$\frac{L}{L_\odot} = \left(\frac{R}{R_\odot}\right)^2 \cdot \left(\frac{T_{\rm eff}}{T_{\rm eff,\odot}}\right)^4 \ . \tag{26}$$

And finally the derivation of the mass of the star is possible:

$$M = g\frac{R^2}{G} \ , \tag{27}$$

where G is the gravitational constant.

3. Results

During this thesis a spectroscopic and photometric analysis of 113 spectra from the follow-up to the HQS survey was performed. The results from this analysis are the atmospheric parameters like temperature $T_{\rm eff}$, surface gravity $\log g$ and helium abundance $\log \mathrm{He/H}$ and the stellar parameters like radius R, luminosity L and mass M which will be examined in this chapter.

3.1. New Binaries

When trying to derive the atmospheric parameters of a star by model fitting, it is important to know whether the star system in question is composed of several constituents i.e. a composite system or if it is a single star. In a composite system the flux of the stars effectively overlaps and the distinction between the contribution of the different stars to the overall spectrum becomes difficult.

During observations made in the spectroscopic follow-up to potential hot subdwarfs in the Hamburg Quasar Survey, the spectra were classified to be single or composite with a cooler companion based on four criteria:

- The existence of the CaII H+K absorption lines
- G-band absorption typical for G-class stars
- The presence of the MgI Triplett absorption feature
- An overall flat flux continuum

Based on these criteria Edelmann et al. (2003) determined 18 stars of the sample to be composite systems.

With the conduction of several comprehensive stellar surveys over the last two decades most notably the near-infrared survey 2MASS and the mid-infrared survey WISE the search for cool companions to our hot subdwarfs can be performed more quantitatively as they can detect the wavelength regions where cool stars emit light maximally.

By running SED Fits on the available photometric catalogs for the sample four more composite systems can be added to the list of binaries which have not been classified as composite in Edelmann et al. (2003). One of these systems HS0016+0044 however has since already been identified to be a binary by Girven et al. (2012) whereas the other three systems HS0232+3155, HS1824+5745 and HS2151+0857 have not been identified as binaries in the literature. Table 4 of

appendix A gives a list of the composite systems in this sample and their stellar parameters.

In Figure 6 I show SED fits for two of these composite system, where the hot subdwarf dominates the radiation at lower wavelengths whereas the cooler companion dominates the higher wavelengths. The first SED shows a cooler possible K-type main-sequence star companion and the other one a hotter companion of possibly F-type. However as we will see the spectral fits to determine the temperatures which are used in the SEDs have to be considered with caution so that exact values for binary temperatures are also to be treated with caution depending on how much the companion contributes to the flux in the spectral range covered by the spectrum which depends on the spectral type of the companion. In Figure 7 I show the SED fits for the other two new binaries.

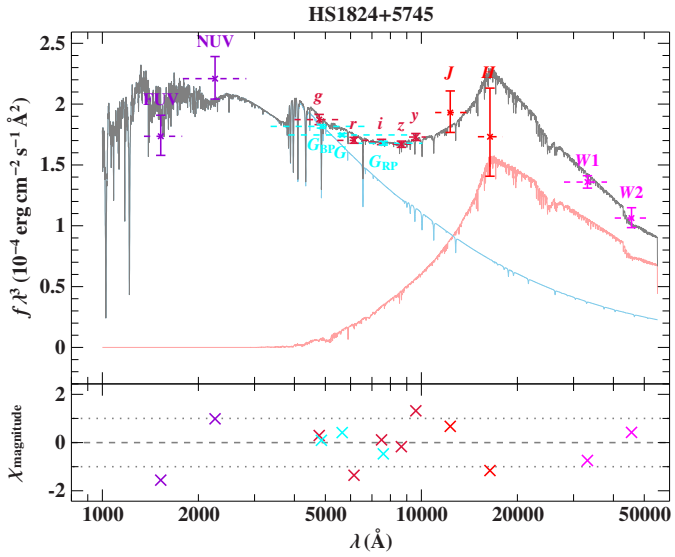

(a) SED fit for the new discovered binary HS1824+5745

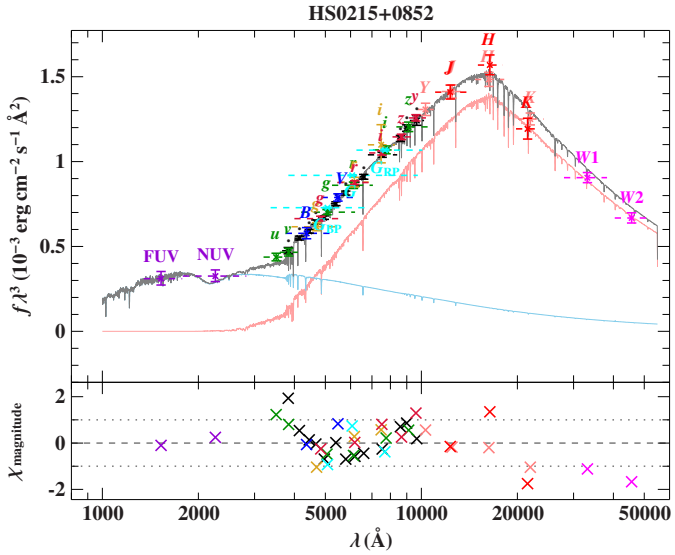

(b) SED fit for the already known binary HS0215+0852

Figure 6: SEDs for two of the binary systems. For each of the two systems the plot in the top displays the flux times the wavelength cubed against the wavelength. The data points with error bars are the photometric measurements in the annotated photometric band. In blue is the contribution from the hot subdwarf, in red is the contribution from the cooler companion and the total flux is shown in black. The lower plot shows the residue in terms of magnitudes.

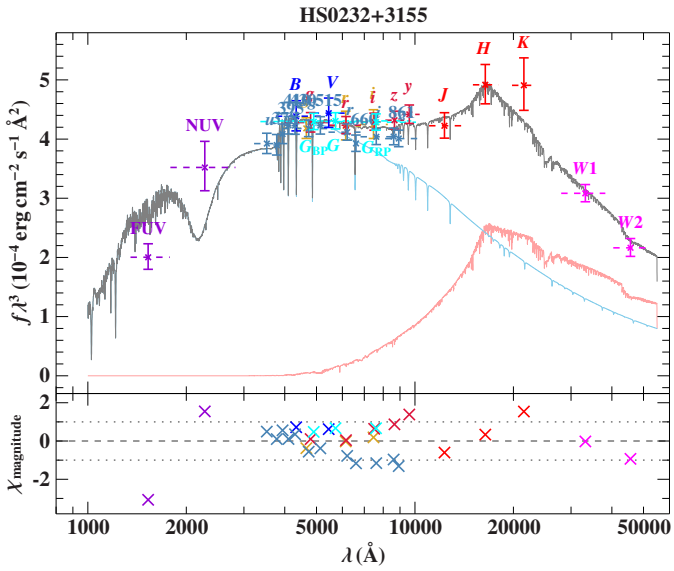

(a) SED fit for the new discovered binary HS0232+3155

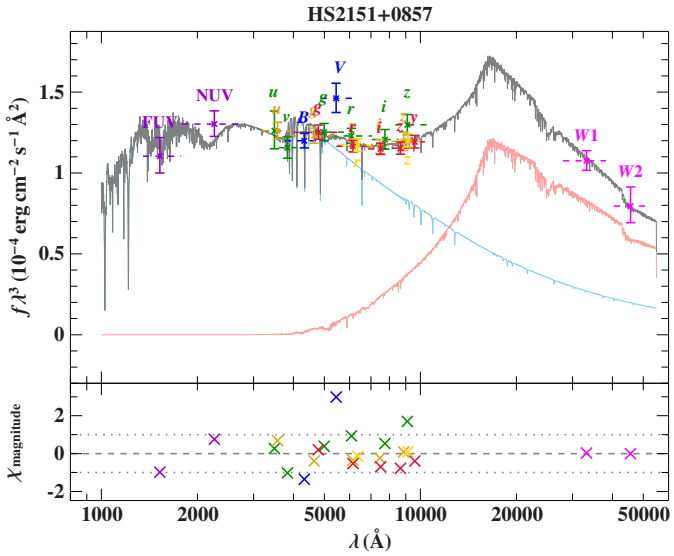

(b) SED fit for the new discovered known binary HS2151+0857

Figure 7: SEDs for the other two new binary systems. The plot in the upper panel displays the flux times the wavelength cubed against the wavelength. The data points with error bars are the photometric measurements in the annotated photometric band. In blue is the contribution from the hot subdwarf, in red is the contribution from the cooler companion and the total flux is shown in black. The lower plot in either panel shows the residue.

3.2. Atmospheric Parameters from Spectroscopy

3.2.1. Spectroscopic fit

Now with the completed identification of composite systems in the sample the spectroscopic fits can be performed. The spectra of all systems whether or not they are single or composite were fitted with theoretical models for single stars which means that for the rest of the analysis the focus will be on apparently single stars as the parameters obtained from the spectra of composite systems are not trustworthy.

As an example the fit to the spectrum of HS0740+3734 is shown in Figure 8 which was taken with the TWIN spectrograph in 1993. The spectrum shows the typical strong Hydrogen Balmer lines of a sdB star. In Figure 9 the spectroscopic fit of the blue channel to two other stars is shown. The first is for HS2208+2718, a sdB with a low helium abundance of below the modelgrid $\log \mathrm{He} = -5.05$, the second one is for HS0546+8009, a sdOB with a high helium abundance of $\log \mathrm{He} = -1.994^{+0.019}_{-0.02}$.

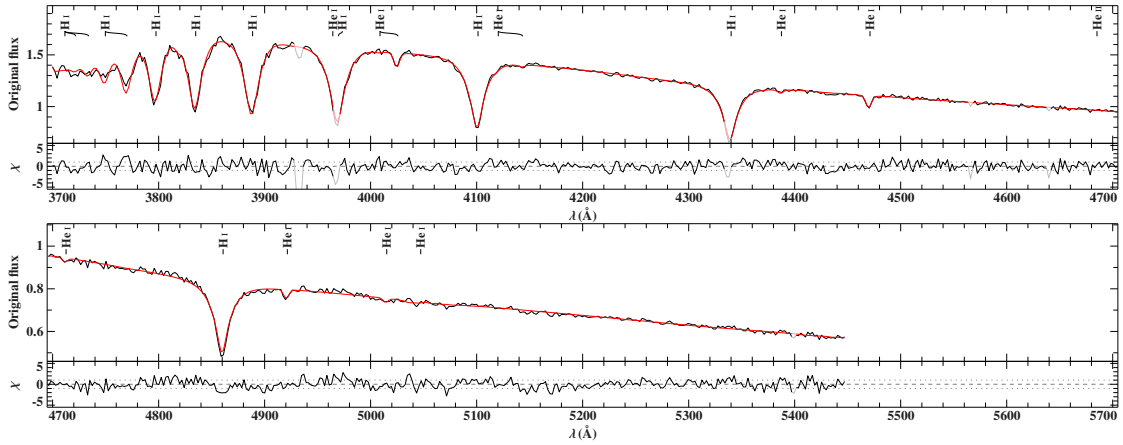

(a) Spectroscopic fit for the blue spectrum channel of HS0740+3734

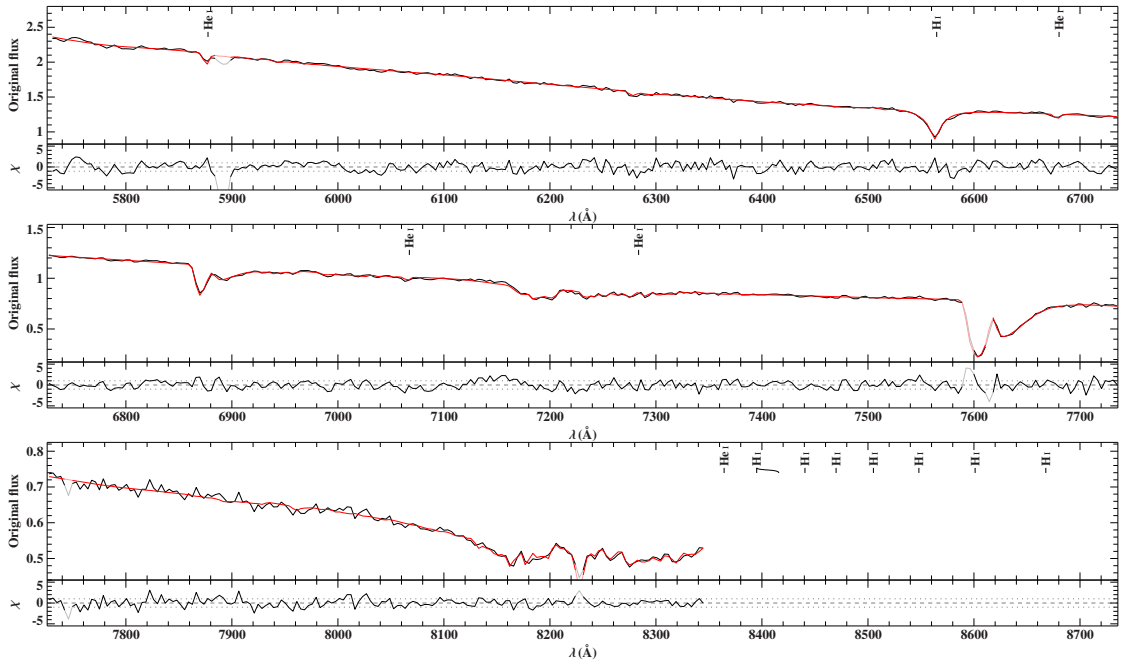

(b) Spectroscopic fit for the red spectrum channel of HS0740+3734

Figure 8: Spectroscopic fit to the spectrum of the sdB HS0740+3734 with a temperature of $T_{\rm eff} = 22\,000 \pm 700$ K and surface gravity of $\log g = 5.27 \pm 0.11$. The upper panel shows the blue channel of the TWIN spectropraph from 3700 Å to 5450 Å and the lower panel shows the red channel from 5730 Å to 8350 Å. The black plot shows the measured spectra while the red plot depicts the fitted model. The lower panel to each plot shows the residual. The hydrogen Balmer absorption lines are clearly visible as well as the HeI absorption lines. At higher wavelengths like 6880 Å or 7600 Å the telluric absorption features are visible as well. A model for absorption by the Earth atmosphere is included in the fit.

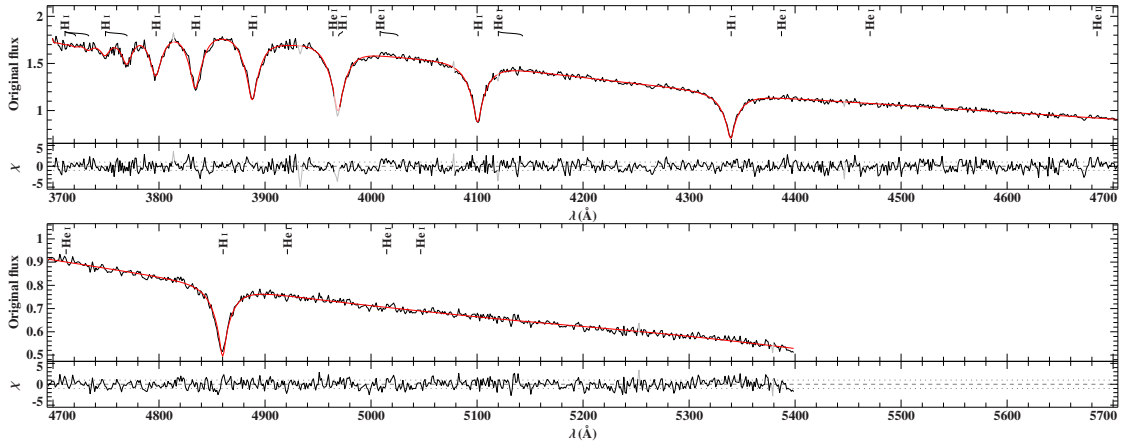

(a) Spectroscopic fit for the blue spectrum channel of HS2208+2718

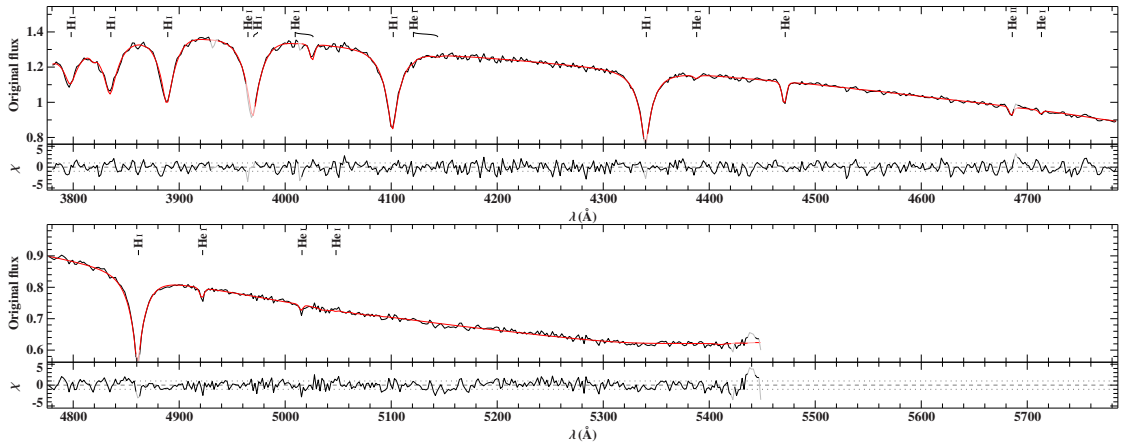

(b) Spectroscopic fit for the blue spectrum channel of HS0546+8009

Figure 9: Spectroscopic fit to the blue part of the spectrum of the sdB HS2208+2718 in the upper panel and of sdOB HS0546+8009 in the lower panel. The sdB HS2208+2718 shows no visible helium lines, whereas the sdOB HS0546+8009 shows HeI lines as well as a HeII line.

3.2.2. Atmospheric parameters from HQS follow-up

With the spectroscopic measurements from the follow-up to the Hamburg Quasar Survey and the tools of spectral analysis, we can now take a look at the atmospheric parameters of the stars within this sample. The quantities of interest here are the stellar effective temperature T_{eff}, the surface gravity $\log g$ and the helium abundance of the photosphere $\log \mathrm{He}$. The atmospheric parameters are tabulated in Table 1 of Appendix A.

In Figure 10 a plot of $\log g$ over T_{eff} is shown, which is typically called a Kiel-

diagram, of all stars in the sample that are not identified as composite systems. The Helium abundance of the stars are also displayed as a color.

The position of stars in the Kiel-diagram depends on the spectral type of the stars and their current evolutionary status. Therefore what is plotted as well are theoretical evolutionary tracks for hot subdwarfs from Dorman, Rood, and O'Connell (1993), specifically the tracks for the Zero-Age-Extreme-Horizontal-Branch (ZAEHB) and the Terminal-Age-Extreme-Horizontal Branch (TAEHB) as well as the core Helium burning Main-Sequence (HeMS) from Paczynski (1971).

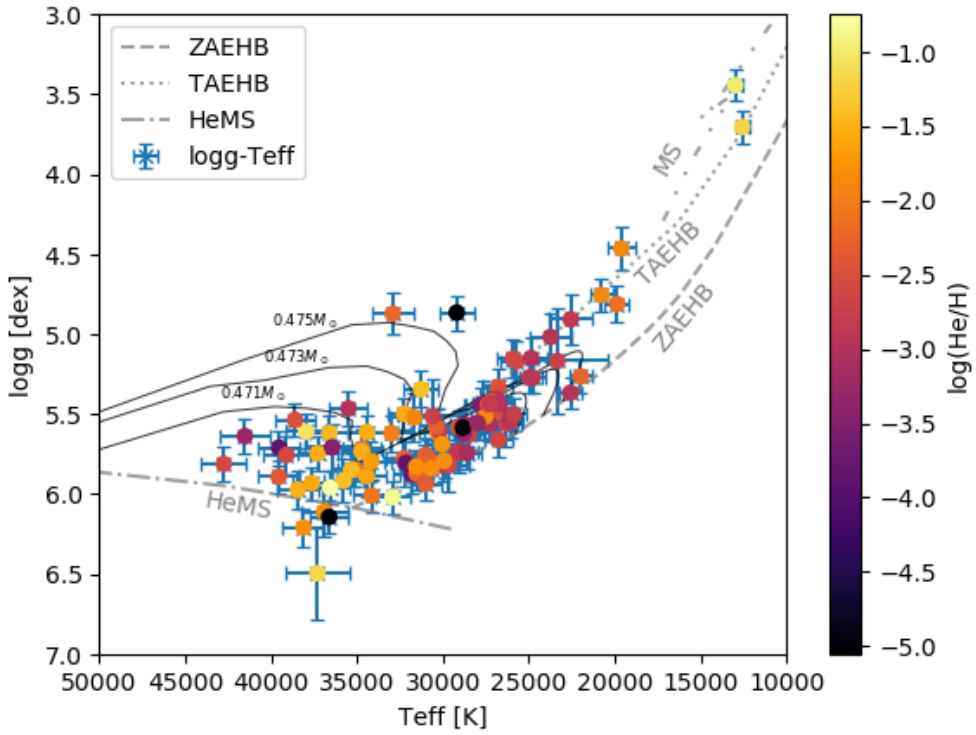

Figure 10: Kiel-diagram for all non-binary stars in the sample which means it is a plot of surface gravity against temperature. The helium abundance is additionally indicated with a color. The ZAEHB, TAEHB tracks and evolutionary sdB star models for masses of 0.471 $M_{\odot}$, 0.473 $M_{\odot}$ and 0.475 $M_{\odot}$ from Dorman, Rood, and O'Connell (1993) and the HeMS track from Paczynski (1971) as well as the main sequence evolutionary track for a star with 5 solar masses from Schaller et al. (1992) are also plotted in gray.

There are a few different groupings distinguishable. For one on the lower end

of the temperatures we can find two systems that apparently do not belong to the Extreme Horizontal Branch. One of these two stars, HS2131+0349, has parameters that are most consistent with being a normal main-sequence B-class star. The other star HS1556+6032 also shows typical B-star atmospheric parameters but its stellar parameters which are derived in section 3.3 are not compatible with a main-sequence star and could possibly be a helium core white dwarf progenitor (Heber, 2016b).

Then at higher surface gravities and temperatures the Blue Horizontal Branch begins and then transitions into the Extreme Horizontal Branch at temperatures around roughly 20 000 K (Heber, 2009).

The bulk of stars in this sample however are hot subdwarfs. The sdBs make up most of the stars from temperatures of around 20 000 K to 35 000 K. sdOBs are also present from temperatures above approximately 30 000 K and are characterized by the presence of weak HeII absorption lines which are not found in sdBs. sdOs which show HeII lines with no or very weak HeI lines are not a part of this sample.
Beyond distinguishing different spectral types, there are further observations to be made from plotting the Kiel-diagram.

First the sample stars from 20 000 K to 30 000 K seem to follow a linear relationship between $\log g$ and T_{eff} and then as the temperatures increase beyond 30 000 K the temperature-logg pairs spread out over a larger area in the T_{eff}-logg plane.

Second the helium abundance relative to the hydrogen abundance log(He/H) increases with an increase in temperature which also corresponds to the transition from sdB stars to sdOB stars.

Last there are a few outliers from the overall distribution in the stars in the teff-logg plane. HS1842+6557 is the star with the highest surface gravity of 6.5±0.3 dex which is likely to be explained by this spectrum having among the worst SNRs of the sample. The other two outliers (HS1736+8001 and HS0941+4649) which are the ones at temperatures around $T_{\mathrm{eff}} = 30\,000$ K have relatively low surface gravities ($\log g = 4.87 \pm 0.11$ dex and $\log g = 4.87 \pm 0.13$ dex) for their temperatures and could be currently evolving through this region as the evolutionary tracks of Dorman, Rood, and O'Connell (1993) show. HS1736+8001 also has a very low helium abundance at below the atmosphere modelgrid coverage which means that helium absorption lines are not visible at all within the achieved signal-to-noise ratio

Lets take a closer look at only the sdB stars. In Figure 11 the Kiel-diagram for nonbinary sdB stars is shown. As the plot shows most sdBs make up the largest subgroup of the sample. Most sdBs clump up around temperatures from 25 000 K to 32 000 K. However there are also a few hotter sdBs with temperatures up to 40 000 K like for example HS1843+6953 ($T_{\mathrm{eff}} = 41\,500 \pm 1500$ K).

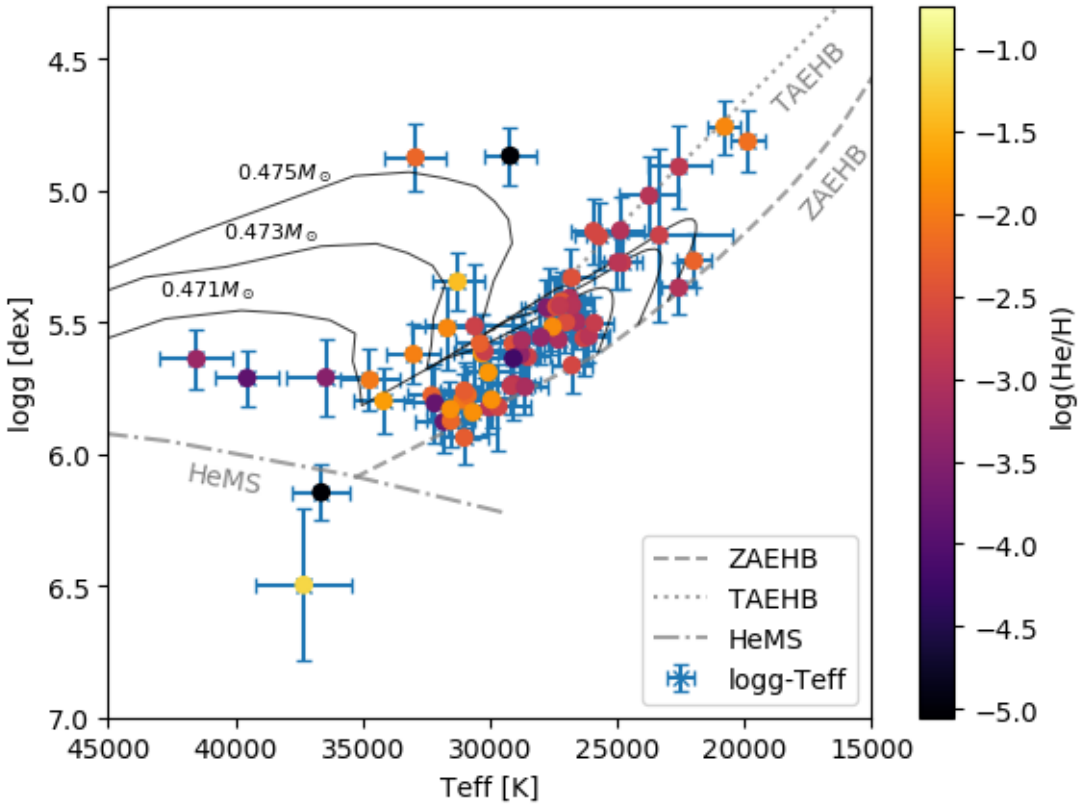

Figure 11: Plot of surface gravity against temperature for all non-binary sdB stars as well as the ZAEHB, TAEHB and evolutionary models for sdB stars with masses of 0.471 $M_{\odot}$, 0.473 $M_{\odot}$ and 0.475 $M_{\odot}$ from Dorman, Rood, and O'Connell (1993) and the He-MS track from Paczynski (1971).

One interesting trend already visible in the plot is that the helium abundance and temperature of the sdBs are correlated. To explore this further log(He/H) is plotted against T_{eff} in Figure 12. The relationship where a higher temperature equals a higher helium abundance is clearly visible. However there also seem to be two groups of stars where one has an overall lower helium abundance but still shows the aforementioned correlation. The stars with a helium abundance of

$\log \mathrm{He/H} = -5$ are to be seen as upper limits as the atmosphere models do not extend beyond these abundances.

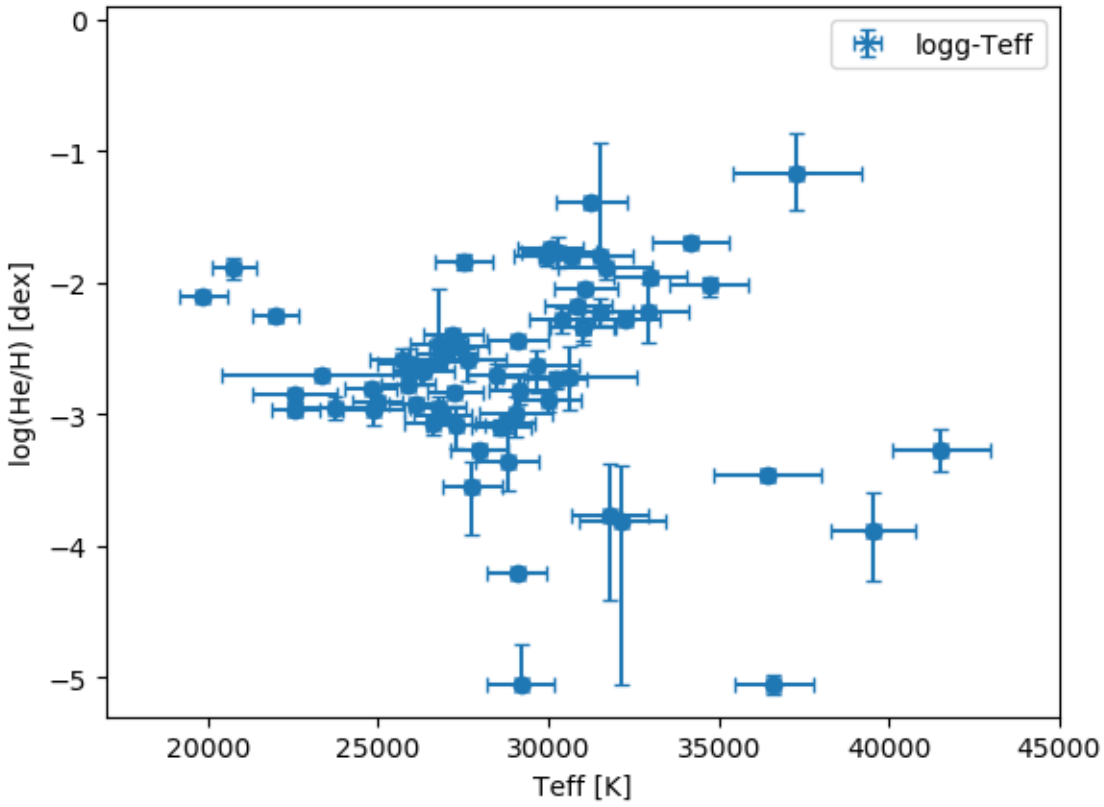

Figure 12: Plot of helium abundance against temperature for the sdB stars in the sample. The horizontal line at approximately $\log \mathrm{He/H} \approx -1$ represents the solar helium abundance.

When one is including all the stars from the sample that belong to the EHB then this relationship becomes even clearer as is shown in Figure 13. This overall relationship between helium abundance and temperature is also apparent in Edelmann et al. (2003) which was also the first study of hot subdwarfs to show this feature.

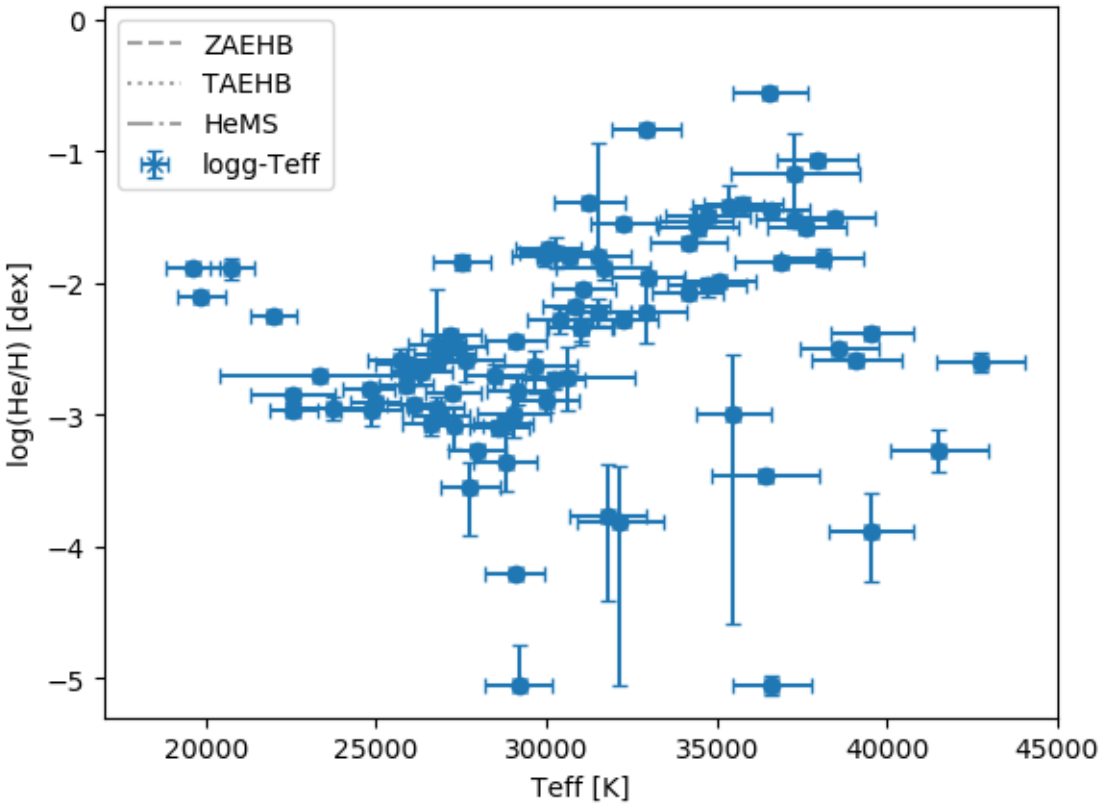

Figure 13: Plot of helium abundance against temperature for all stars in the sample that belong to the EHB. The horizontal line at approximately $\log \mathrm{He/H} \approx -1$ represents the solar helium abundance.

3.2.3. Comparison with Edelmann et al. (2003)

As atmospheric parameters, i.e. T_{eff}, $\log g$ and $\log \mathrm{He}$ were also derived for this sample in Edelmann et al. (2003) however with a different fitting method and different model spectra a comparison between the atmospheric parameters from this analysis and the analysis of Edelmann et al. (2003) is appropriate.

The first parameter for this comparison will be the temperature. In Figure 14 the relative difference in effective temperatures $(T_{\mathrm{this}} - T_{\mathrm{Edelmann}})/T_{\mathrm{this}}$ is plotted against the temperature from this analysis T_{this}. This comparison is done for every star that was identified as non-binary as no parameters were derived for binary stars in Edelmann et al. (2003).

For the two stars below a temperature of 15 000 K which are the two B-stars the

derived temperatures are in agreement within the uncertainties. For the stars with temperatures ranging from 20 000 K to 25 000 K the differences become larger. For the two stars HS1839+7951 and HS1926+6946 which have temperatures around 23 000 K and the large error bars the discrepancy may come from the subpar signal-to-noise-ratio which when combined with the different fitting method could lead to different results. For the stars with temperatures 25 000 K a trend in the temperature differences seems to appear. For temperatures above 34 000 K the temperatures from this analysis become higher than the temperatures from Edelmann et al. (2003) and for temperatures below 34 000 K the derived temperatures from this analysis are smaller than the temperatures from Edelmann et al. (2003). This could be due to the different models used in the analysis. In Edelmann et al. (2003) there are 3 model grids used for different temperature ranges. For temperatures above 35 000 K NLTE models are used. For temperatures between 27 000 K and 35 000 K the mean of a fit with LTE and NLTE models is used and pure LTE models are utilized for temperatures below 27 000 K. This is in contrast to this analysis where one homogeneous model grid is used based on a hybrid LTE/NLTE approach as described in subsection 2.1 which includes detailed metal line blanketing. This could mean that pure NLTE models can underestimate temperatures whereas pure LTE models can overestimate the temperatures of hot subdwarfs in these temperature regions.

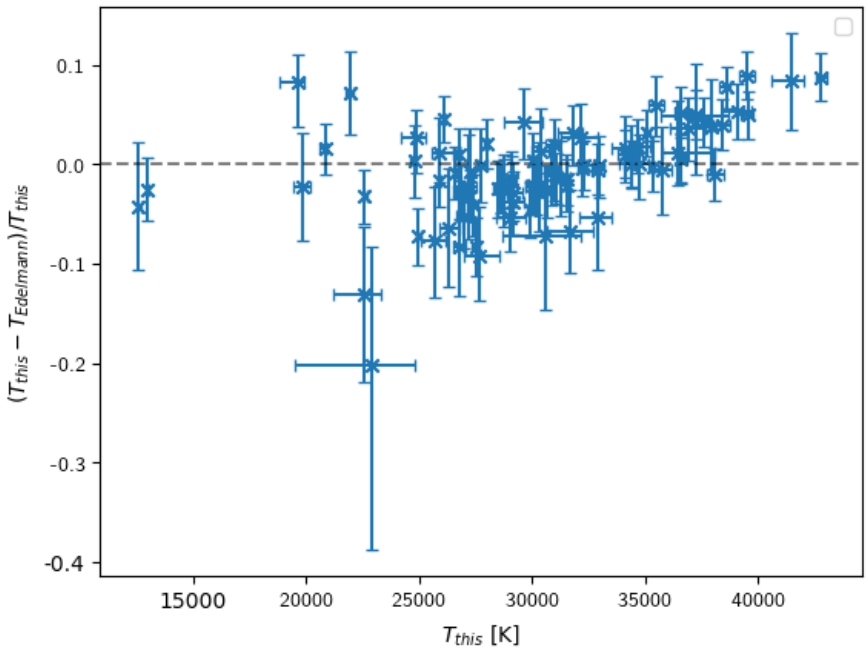

Figure 14: Plot of the differences in temperatures when comparing the results from this analysis to the analysis of Edelmann et al. (2003). The black dashed line indicates no difference in temperatures.

The comparison of the surface gravities is shown in Figure 15. Here the surface gravities are in agreement with each other for the two B-stars at $\log g < 4$ and for the bulk of the stars from $\log g = 5.3$ to $\log g = 6.5$. For the surface gravities around $\log g = 5$ there are again the two systems HS1839+7951 and HS1926+6946 with large errors due to the signal-to-noise ratio. The system with the largest deviation is HS0941+4649 at a relative difference of about -20%. The temperature difference for this system is not significant at about -5% which could mean that the difference here is due to the different fitting method, i.e. which Balmer lines are considered in the fit of the spectrum taken with the B&C spectrograph. A spectroscopic fit to a SDSS spectrum of HS0941+4649 also results in $\log g = 5.078^{+0.027}_{-0.023}$ which is much closer to the surface gravity from this analysis $\log g = 4.87 \pm 0.13$ than the surface gravity from Edelmann et al. (2003) $\log g = 5.8 \pm 0.2$.

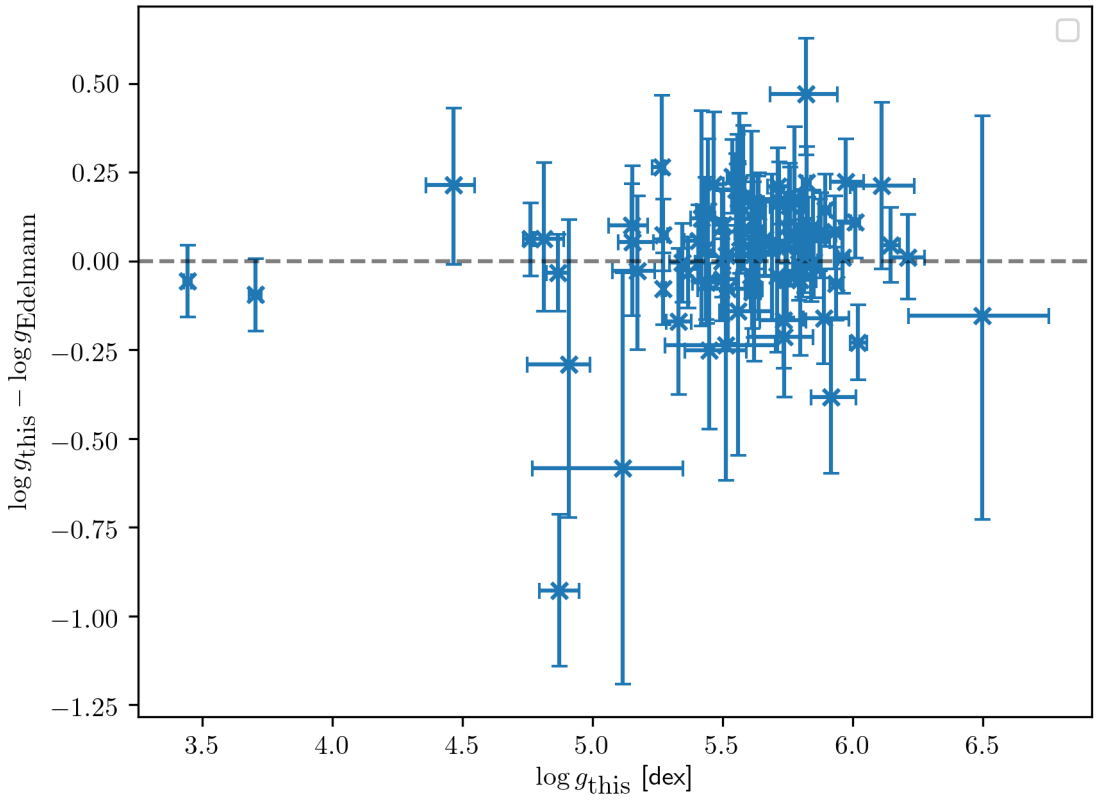

Figure 15: Plot of the differences in surface gravities when comparing the results from this analysis to the results of Edelmann et al. (2003). The black dashed line indicates no difference in surface gravity. [Revised]

The plot of the differences for the helium abundances is shown in Figure 16. Here the parameters from both this analysis and from Edelmann et al. (2003) are in agreement over the whole abundance range. The higher errors for lower helium abundances come from the fact that the lower the helium abundance is the weaker the helium lines get which makes a fit more difficult.

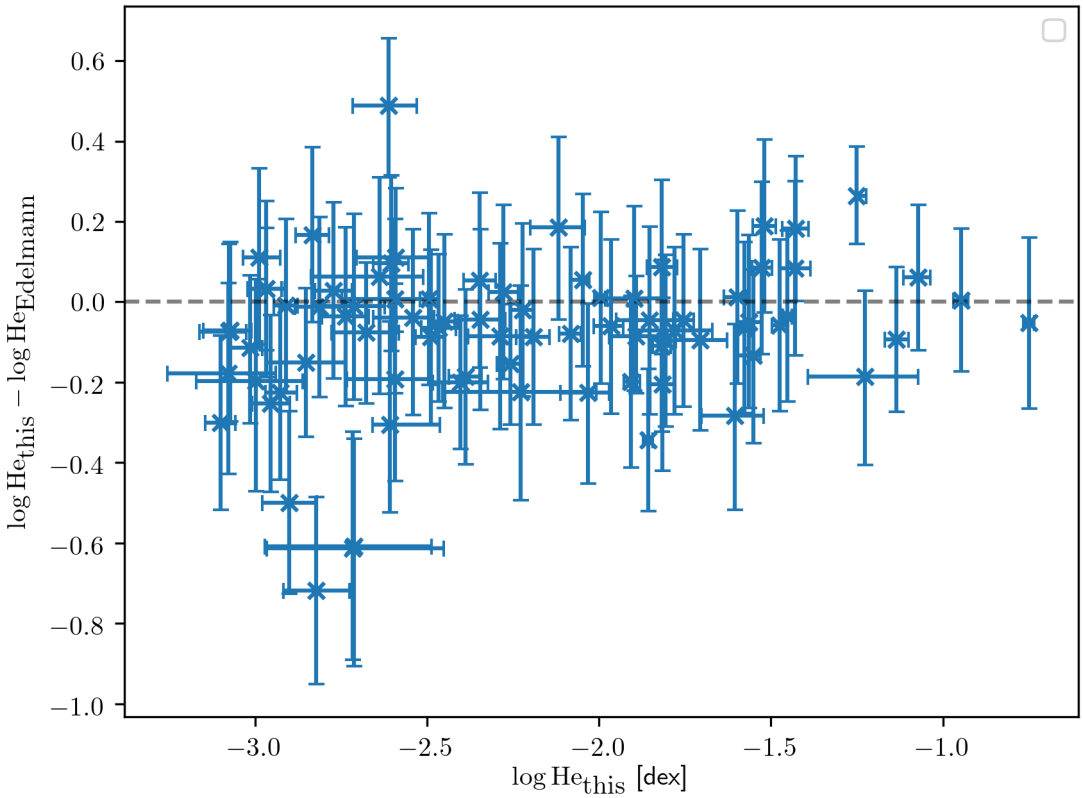

Figure 16: Plot of the differences in helium abundances when comparing the results from this analysis to the results of Edelmann et al. (2003). The black dashed line indicates no difference in helium abundance. Lower helium abundances $\log \mathrm{He} < -3.2$ are not shown as their determination becomes uncertain due to weaker spectral lines. [Revised]

3.2.4. Comparison with SDSS/LAMOST spectra

The SDSS (Blanton et al., 2017) and LAMOST (Cui et al., 2012) missions conduct spectroscopic surveys of stars and several of the stars in this sample also have spectra in the SDSS data release 17 (Abdurro'uf et al., 2022) and/or the LAMOST data release 8. These spectra were downloaded and analysed with the same methods as the spectra from the HQS survey and the atmospheric parameters from the SDSS/LAMOST spectra will now be compared to the results from this analysis. The derived atmospheric parameters for the SDSS/LAMOST spectra are listed in Table 2 of appendix A.

In Figure 17 the relative differences in the temperatures of the HQS spectra to

the SDSS/LAMOST spectra is shown. Most temperatures are in agreement with each other within 10%. The outliers which are beyond 10% difference are all from LAMOST spectra with lower signal-to-noise ratios.

The relative differences in the surface gravities is shown in Figure 18. Here most surface gravities are in agreement with each other within 10% as well with the two spectra beyond this being LAMOST spectra. This allows the conclusion that the results from the HQS spectra and the SDSS/LAMOST spectra show no significant systematic differences.

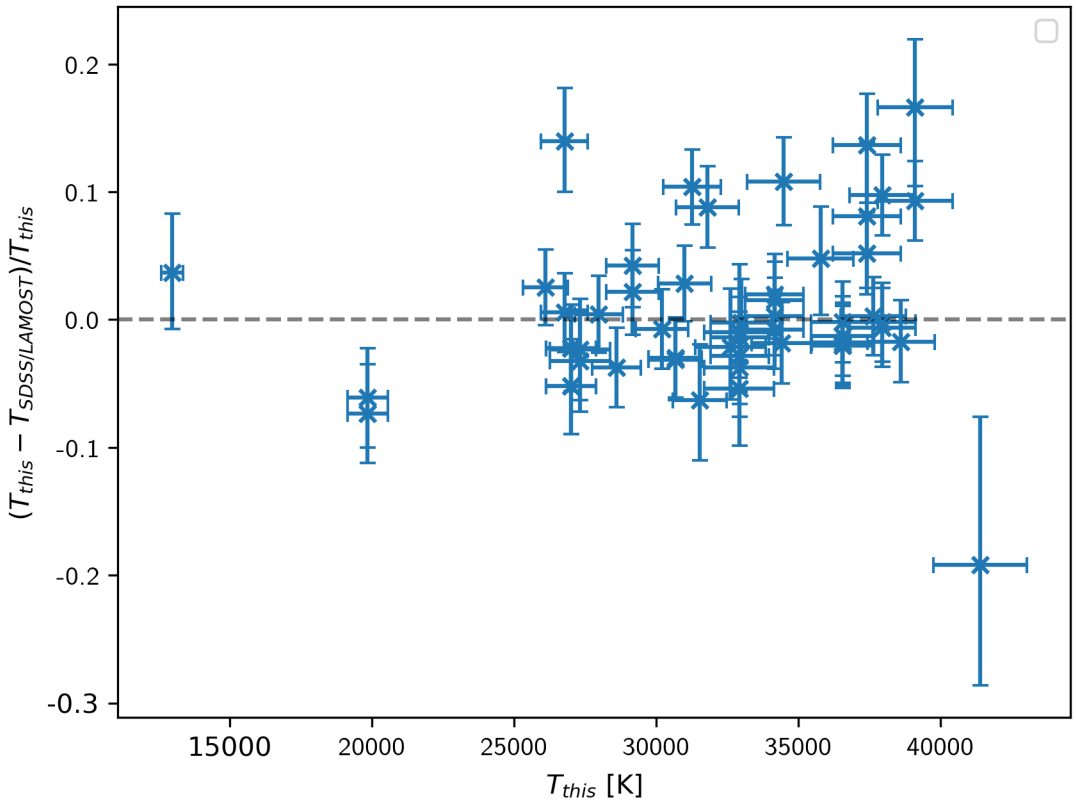

Figure 17: Plot of the differences in temperatures when comparing the results from the HQS spectra to the SDSS/LAMOST spectra. The black dashed line indicates no difference in temperatures. [Revised]

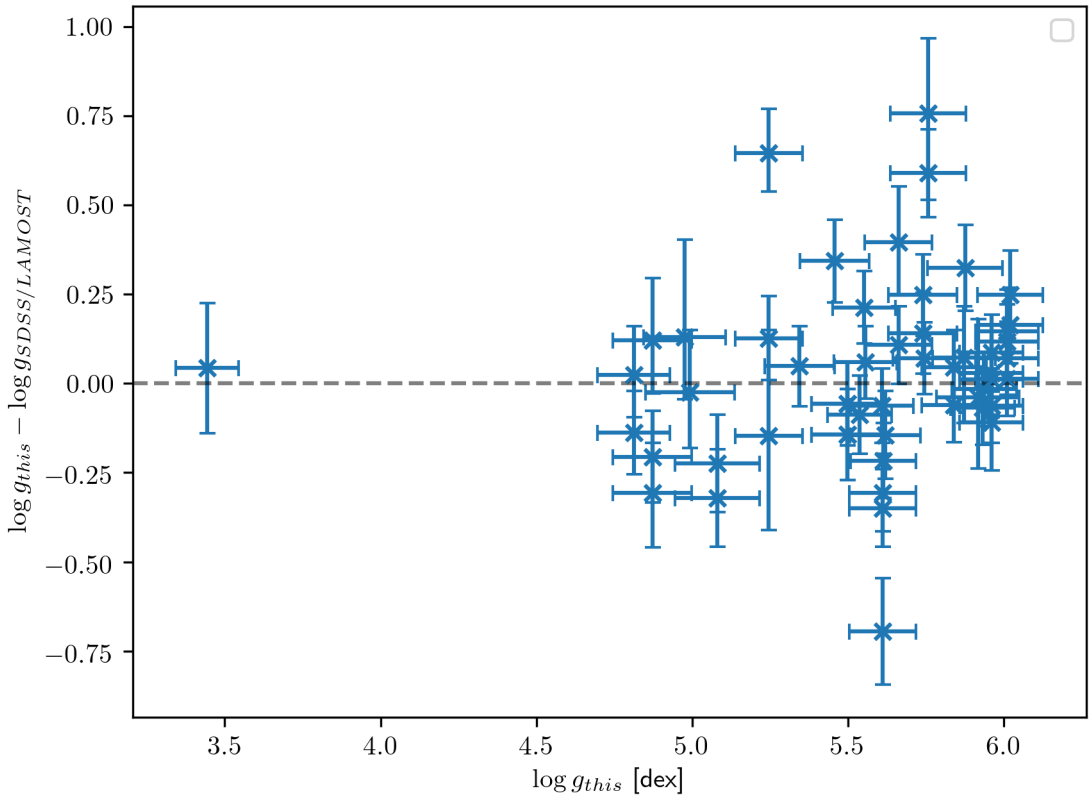

Figure 18: Plot of the differences in surface gravities when comparing the results from the HQS spectra to the SDSS/LAMOST spectra. The black dashed line indicates no difference in surface gravities. [Revised]

3.3. Stellar parameters from Photometry and Parallax

Now, if we combine the determined parameters from the spectra , i. e. the atmospheric parameters temperature and surface gravity, with the information of the photometric measurements by fitting the SEDs we derive the angular diameter Θ of the star and constrains on the interstellar reddening by means of the colour excess $E(44-55)$. The stellar parameters Radius R, Mass M and Luminosity L can now be determined by using the measured parallaxes $\overline{\omega}$ from the Gaia Mission. The photometric fit data can be found in Table 3 of appendix A.

In Figure 19 the photometric fit is shown for the star HS0740+3734 which is also the same star from the spectroscopic fit example shown in Figure 8. We plot the flux times the wavelength cubed against the wavelength which means that even though the ultraviolet part of this SED is lower in the plot than the

optical part the actual ultraviolet flux is still higher than the optical flux. This SED has good coverage from ultraviolet to the mid-infrared and features like the Balmer jump, where the Balmer series transitions to the continuous energy levels, is visible in the u-band measurements as well as a interstellar reddening of $E(44-55) = 0.0583^{+0.0023}_{-0.0069}$ mag which can be seen in the effect on the ultraviolet flux because the interstellar extinction grows from the infrared to the ultraviolet with a characteristic peak at 2200 Å according to Fitzpatrick (1999).

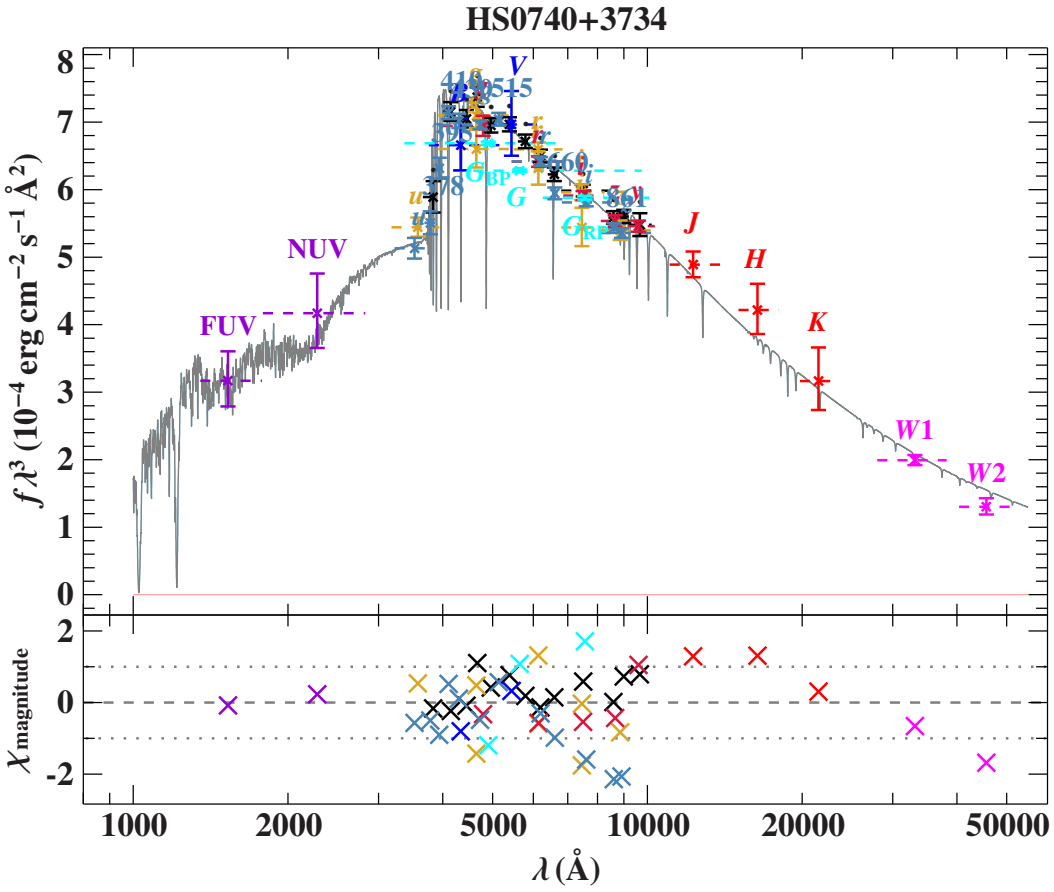

Figure 19: SED for the sdB HS0740+3734. In the upper panel the individual plotted points with errors are the measurements from the many photometric surveys, where the dashed horizontal lines indicate the width of the photometric filters. The solid black line shows the fitted model. The lower panel gives the residual χ.

3.3.1. Trigonometric Parallaxes from Gaia

The parallaxes from the Gaia satellite are at the heart of determining the stellar parameters which means that they are worth a closer look. In Figure 20 the distribution of absolute parallaxes of the stars in the sample is shown in a histogram. We can see that most of our stars have a parallax between 0.6 mas and 0.7 mas or higher which corresponds to distances of 1.7 kpc to 1.4 kpc or closer.

To determine what parallaxes are able to give reasonable distances the uncertainties on the Gaia-parallaxes can be used. The uncertainty on the parallax is mostly dependent on the brightness of the star and how large the parallax actually is. This means that for most of the stars which all have G-Band magnitudes fainter than 13 mag and all except three (HS1051+2933, HS1320+2622 and HS1839+7951) have G-Band magnitudes brighter than 17 mag a reasonable distance can be determined within the accuracy of the Gaia satellite measurements as is shown in Figure 2 of Vallenari et al. (2023). There the typical uncertainties on the parallax is shown dependent on the G-band brightness of the star. For all stars in our sample except HS0028+4408 the uncertainty on the parallax is below 0.1 mas which would be about the maximum uncertainty for stars in our brightness range as shown in the figure.

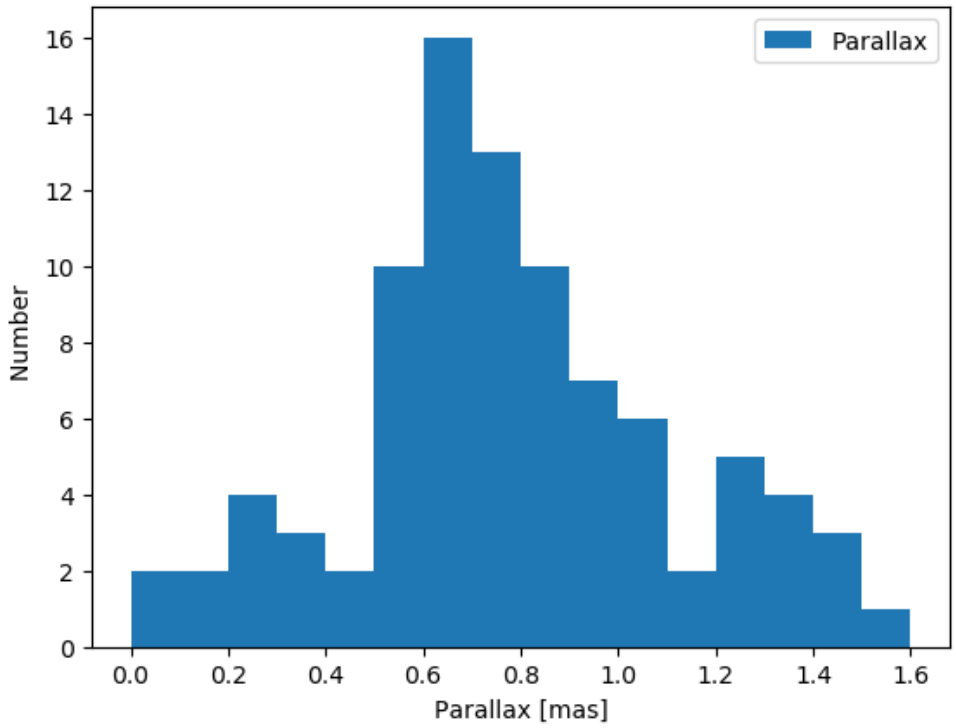

Figure 20: Histogram of the parallaxes from all non-binary stars in the sample. No star has a bigger parallax than 1.6 mas which corresponds to a closest distance of 625 pc.

To derive reasonable stellar parameters from the parallax however not only the absolute parallax needs to be large enough as the parallax uncertainty propagates to the errors of the stellar parameters. This means that the relative uncertainty of the parallax compared to the actual value of the parallax is the chosen tool to constrain the effectiveness of the parallax at providing reasonable stellar parameters. For the following stellar parameters only stars are considered that have a relative parallax uncertainty of a specific percentage of the parallax. For example all stars where the parallax uncertainty is below 10% of the parallax value.

3.3.2. Radius

With the angular diameter from the SED and the parallax of Gaia the radius of the star is calculated with

$$R = \frac{\Theta}{2\overline{\omega}} \tag{28}$$

In Figure 21 a plot of the radius against the temperature of the stars is shown

with all systems that are identified as non-single excluded. The evolutionary Dorman tracks are plotted as well. For this plot a relative parallax error of 10% is chosen.

What can be seen from the plot is that the determined radius-temperature pairs lie in the expected ranges which are predicted by theory and they are scattering close around the theoretical tracks of the ZAEHB, TAEHB and HeMS. The scatter is to be expected from stars that are at different points in their evolutionary lifetime.

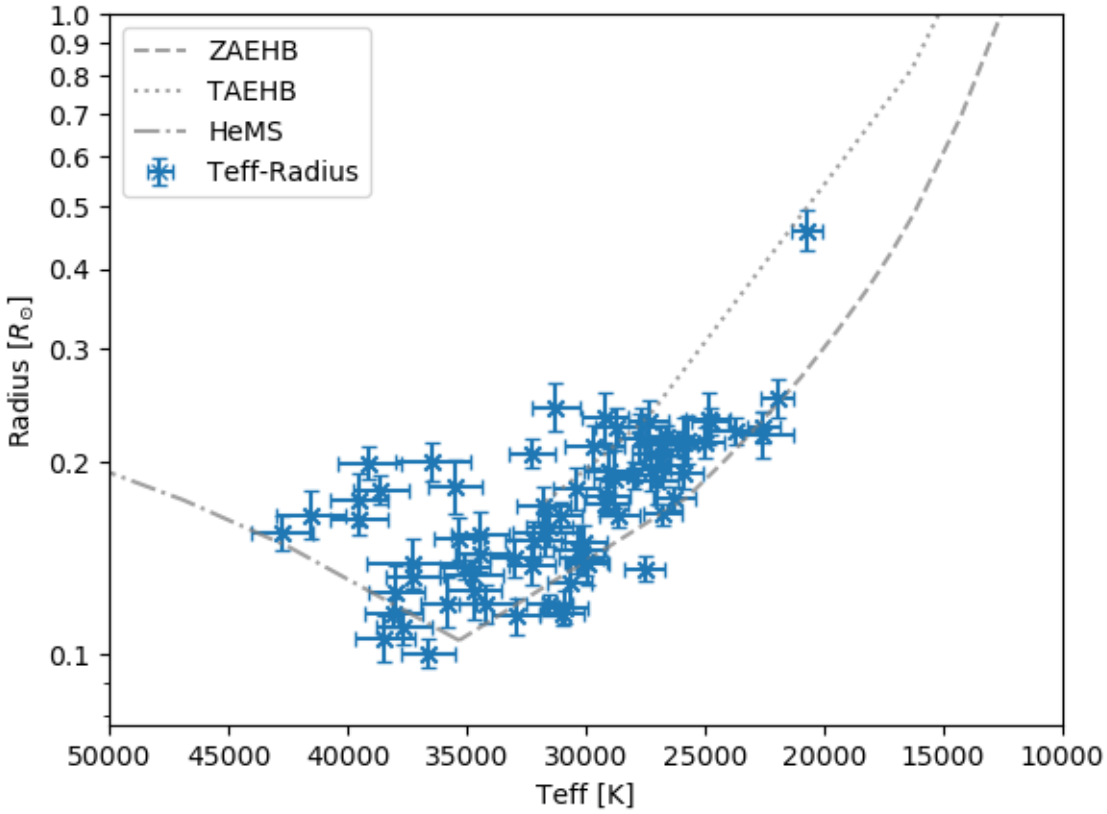

Figure 21: Plot of the radius against the temperature of non-binary stars which have a relative parallax error of below 10%. Plotted as well are the ZAEHB and TAEHB from Dorman, Rood, and O'Connell (1993) and the HeMS from Paczynski (1971). The distribution of the stars largely follows the theoretical models. To mention are the group with bigger radii in the region from 35 000 K to 45 000 K.

Interesting as well is the overall distribution of radii in the sample in a histogram

which is shown in Figure 22. The sample used for this histogram consists of all non-binary stars with a parallax error better than 10%. The radius of all of them except one (HS2224+2618) lie in the range of $0.1\,R_\odot$ to $0.3\,R_\odot$. Here the distribution does not follow a clear trend but lies in a range which is to expected from sdB stars. HS2224+2618 with a radius of $R = 0.46 \pm 0.04\,R_\odot$ also lies at the lower end of the EHB with a temperature of $T_{\rm eff} = 21\,000 \pm 700\,\mathrm{K}$ which could explain the larger radius.

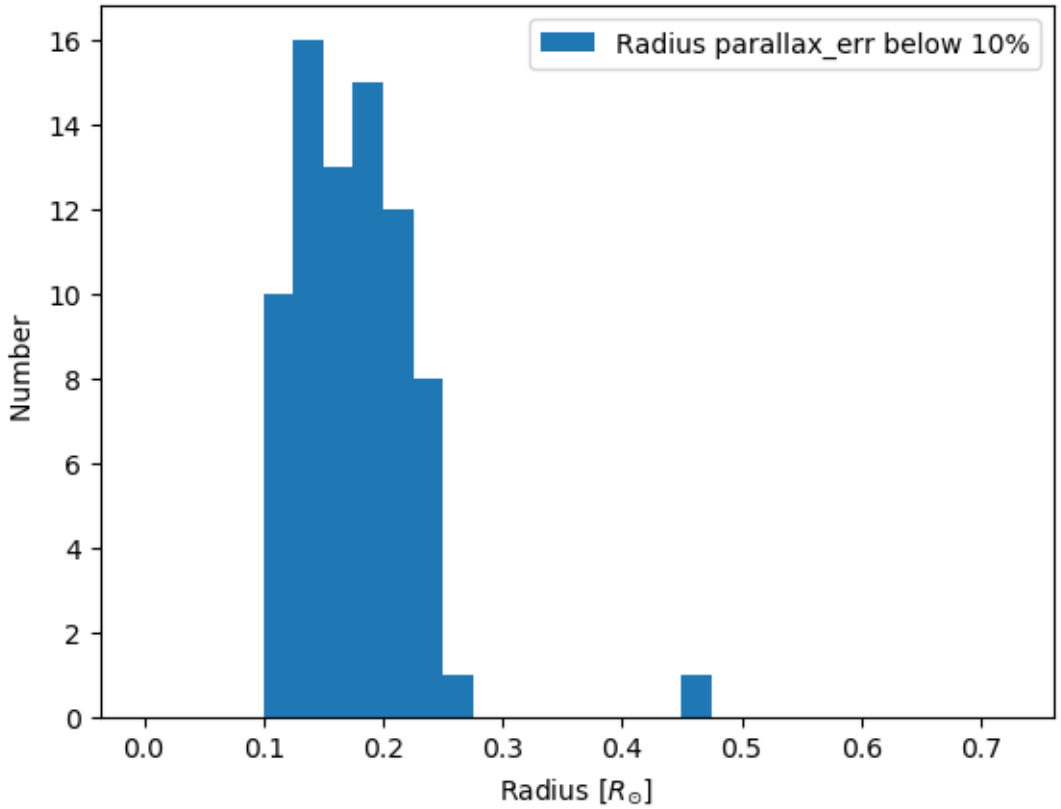

Figure 22: Histogram of the radii from all non-binary stars that have a relative parallax error better than 10%. The radial bin size is chosen to be $0.025\,R_\odot$. Most radii lie in the range of $0.1\,R_\odot$ to $0.3\,R_\odot$.

3.3.3. Luminosity

The luminosity of the star can then be derived from the radius and the temperature of the star with the formula:

$$\frac{L}{L_\odot} = \left(\frac{R}{R_\odot}\right)^2 \left(\frac{T_{\rm eff}}{T_{\rm eff,\odot}}\right)^4 \tag{29}$$

In Figure 23 the plot of luminosity against temperature is shown for all non-binary stars that have a relative parallax error below 10%. The distribution largely scatters in the regions of the luminosity-temperature which are expected from the theoretical models form Dorman, Rood, and O'Connell (1993).

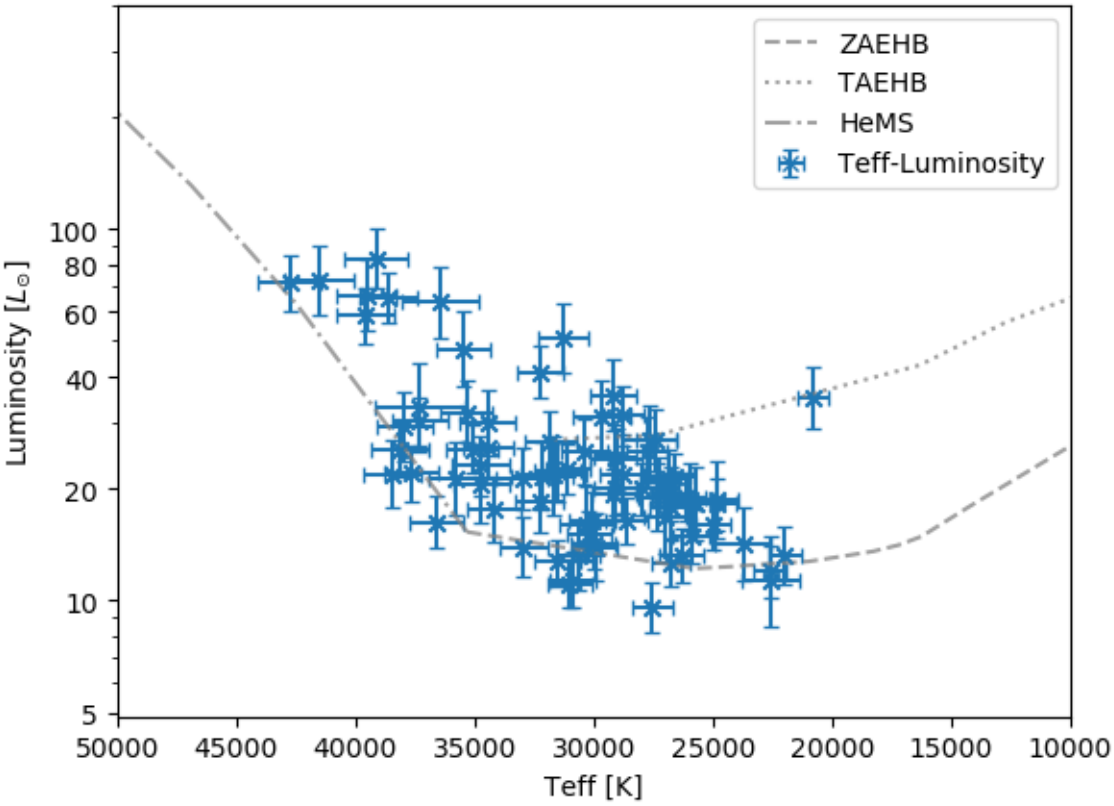

Figure 23: Plot of the luminosities against the temperatures of all non-binary stars which have a relative parallax error below 10%. Plotted as well are the ZAEHB and TAEHB from Dorman, Rood, and O'Connell (1993) and the HeMS from Paczynski (1971). The group of stars with higher luminosities at temperatures above 35 000 K are further developed stars.

To gain further insight into the luminosity parameter the next step is to look at the histogram of the luminosity distribution. This is shown in Figure 24. Here the sample is again all non-binary stars with a relative parallax error below 10%. This distribution shows that most stars in the sample have luminosities in the range of $L = 10\,\mathrm{L}_\odot$ to $L = 30\,\mathrm{L}_\odot$. Only a few of them have luminosities above $L = 40\,\mathrm{L}_\odot$ which consist of the higher temperature subdwarfs.

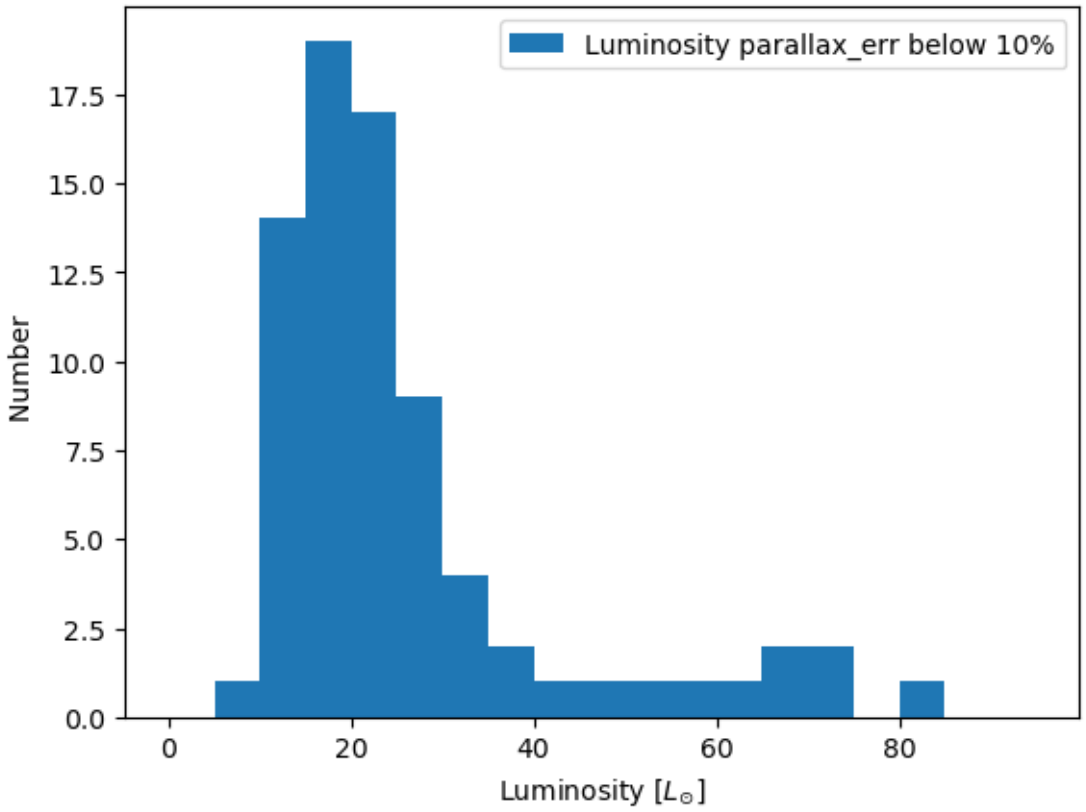

Figure 24: Histogram of the luminosities of non-binary stars with a parallax error below 10%. The bin size is chosen as $5\,\mathrm{L}_\odot$.

3.3.4. Mass

Perhaps the most interesting stellar parameter, especially for theoretical evolutionary models, is the mass of hot subdwarfs. The mass can be calculated with the parameters obtained from the spectroscopic fit and the photometric fits by using Newton's law

$$M = g\frac{R^2}{G} \quad . \tag{30}$$

Here the surface gravity directly influences the mass and because the constrain on the surface gravity from spectroscopic fitting is difficult due to the correlation of temperature and surface gravity the mass determination also becomes more uncertain.

Nevertheless lets take a look at the determined masses. In Figure 25 the histogram of the determined masses of all non-binary stars with relative parallax

errors below 10% is plotted. The histogram shows that most stars have masses in the range of $M = 0.4\,\mathrm{M}_\odot$ to $M = 0.5\,\mathrm{M}_\odot$. However there is scattering around the mean from the lowest masses between $0.1\,\mathrm{M}_\odot$ and $0.2\,\mathrm{M}_\odot$ to the highest masses between $0.8\,\mathrm{M}_\odot$ and $0.9\,\mathrm{M}_\odot$ but as you go away from the mean mass the masses become less and less common. The median of this distribution lies at $M = 0.433\,\mathrm{M}_\odot$ which is close to the theoretical canonical mass of sdB stars which is $M = 0.47\,\mathrm{M}_\odot$ and comes from binary population synthesis models by Han et al. (2003). This mass distribution can be compared to the masses found in V. Schaffenroth et al. (2022) which were also determined by means of spectrocopic and photometric fitting combined with parallaxes from Gaia. Their sample consists of binaries of sdB stars with main-sequence star companions (sdB-MS) and sdB stars with white dwarf companions (sdB-WD). The peak of the sdB mass distribution for the sdB-MS binary systems is close to the canonical mass of sdB which is also the case for the sample of this thesis.

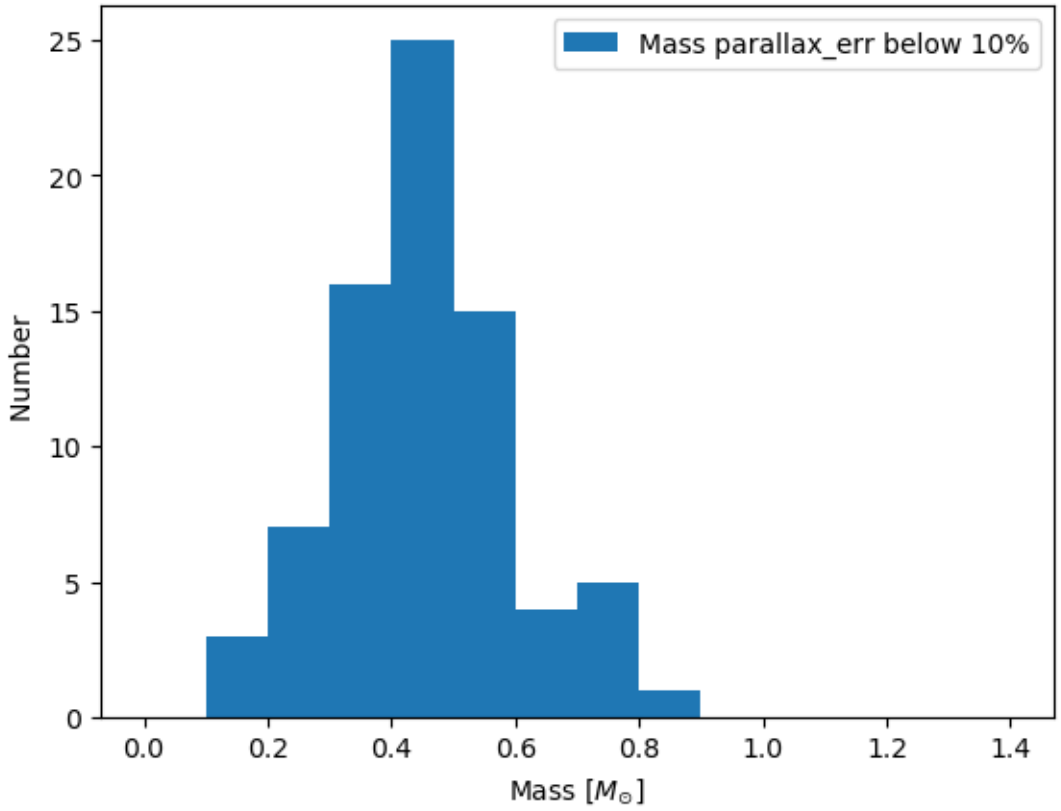

Figure 25: Histogram of the masses of all non-binary stars with relative parallax error below 10%. The bin size is $0.1\,\mathrm{M}_\odot$. The distribution scatters around $0.5\,\mathrm{M}_\odot$.

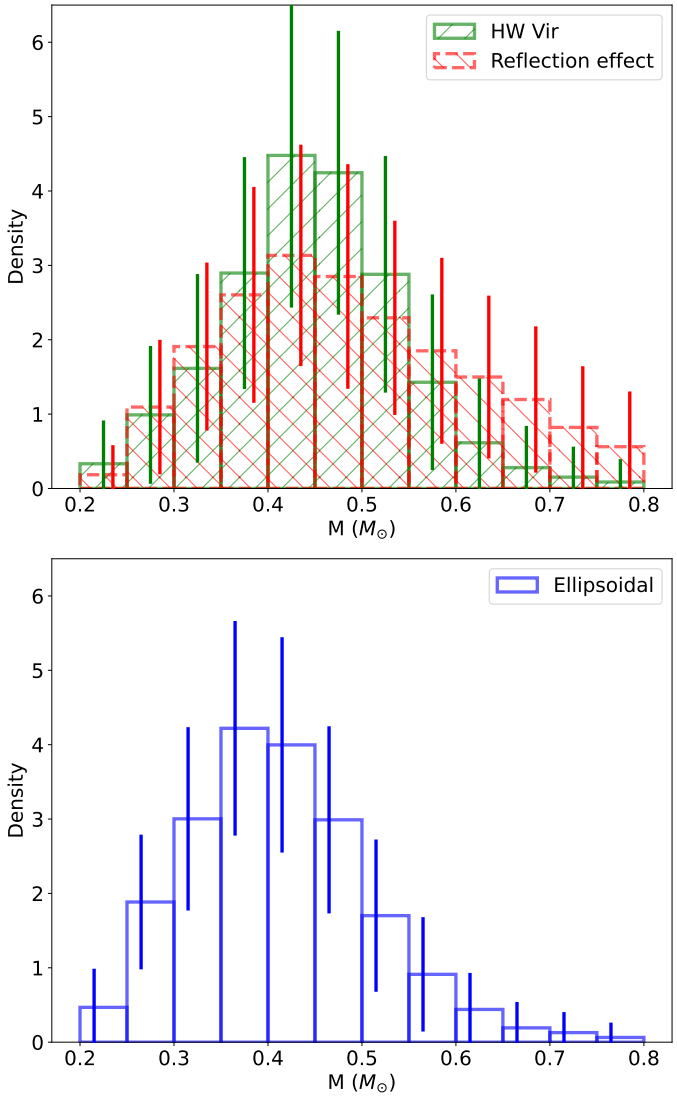

Figure 26: Histogram of the mass distribution found in V. Schaffenroth et al. (2022). The upper panel shows the sdB mass distribution for sdB-MS pairs and the lower panel shows the sdB mass distribution for the sdB-WD pairs.

What would be interesting to look at is how the median of this distribution changes as we change the allowed relative parallax error. This can be seen in Figure 27. This graph shows that the median of the mass distribution does not change significantly when going beyond the allowed parallax error of 10% as only 17% of the non-composite stars have parallax errors worse than 10%.

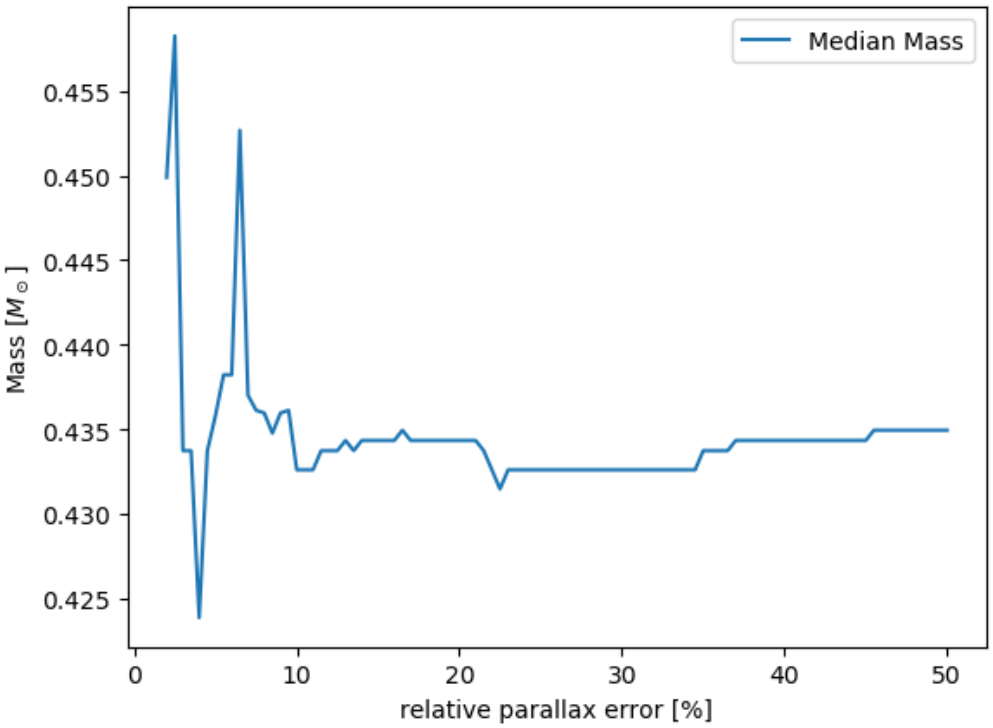

Figure 27: Plot of the median of the mass histogram against the allowed relative parallax err from 0.5 % to 50 %. Beyond the parallax error of 50 % no additional stars are added to the histogram as no non-binary star in this sample has that high relative parallax errors.

3.3.5. Composites

The stellar parameters for the composites in the sample are now considered. In Figure 28 the radius and luminosity of the subdwarf in the composite systems is plotted against the temperature and compared with the ZAEHB, TAEHB and HeMS from Dorman, Rood, and O'Connell (1993) and Paczynski (1971). The temperatures for the subdwarfs come from single-model fits to the spectra. As we can see the position of the stellar parameters radius and luminosity are in agreement with the distribution of non-composite subdwarfs (see Figure 21).

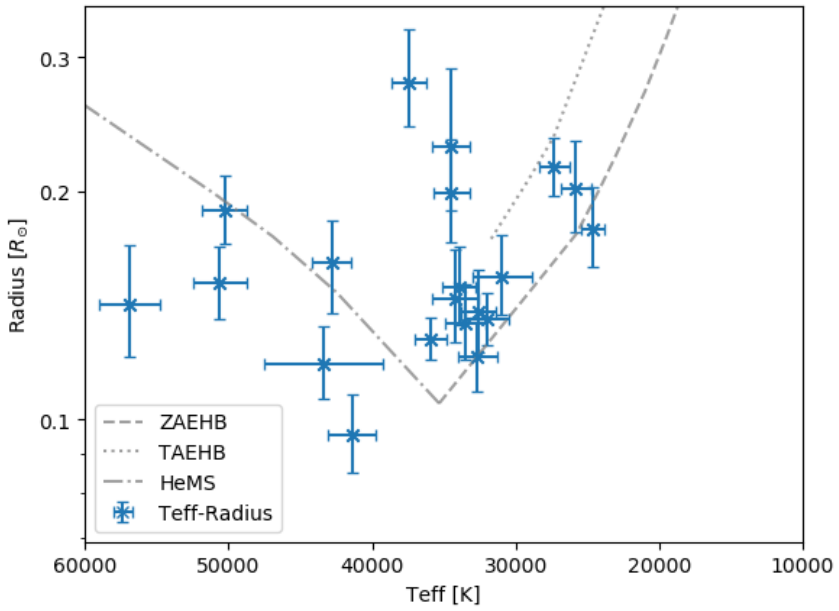

(a) Plot of radius against temperature of the subdwarf in the composite systems.

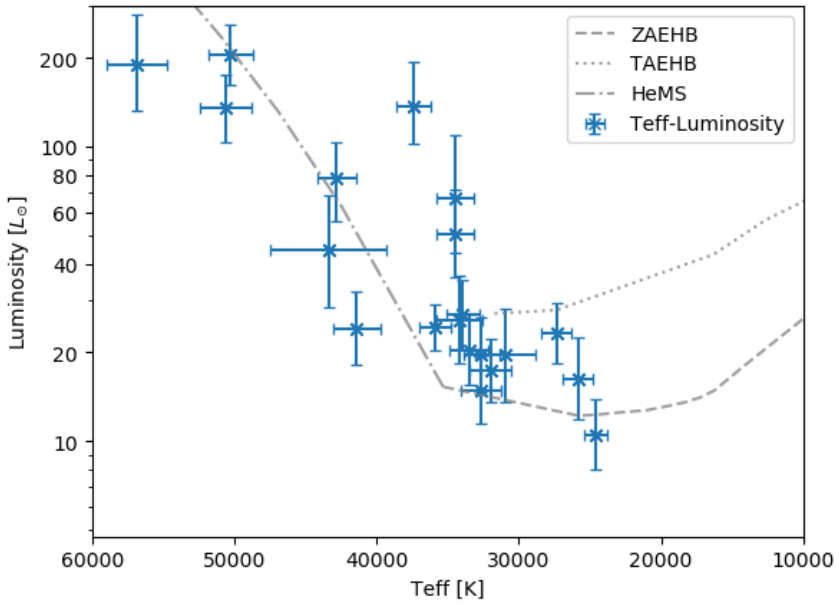

(b) Plot of luminosity against temperature of the subdwarf in the composite systems.

Figure 28: Plots for the stellar parameters against the temperature of the hot subdwarfs in composite systems. The upper panel shows the radius-temperature plot. The lower panel shows the luminosity-temperature plot. The positions of the ZAEHB, TAEHB from Dorman, Rood, and O'Connell (1993) and the HeMS from Paczynski (1971) is plotted as well.

In Figure 29 the radius and luminosity of the main-sequence companion to the hot subdwarf in the composite systems is plotted against the temperature. This is compared to evolutionary models from Girardi et al. (2000) for main-sequence stars with masses of 0.6 $M_{\odot}$, 1 $M_{\odot}$ and 1.3 $M_{\odot}$. The positions of the main-sequence star companions in the HRD (luminosity-temperature plot) and the radius-temperature plot are in agreement with the evolutionary models for relatively unevolved stars that are close to the zero-age main-sequence with masses between between 0.6 and 1.3 $M_{\odot}$ spectral types of F to late K.

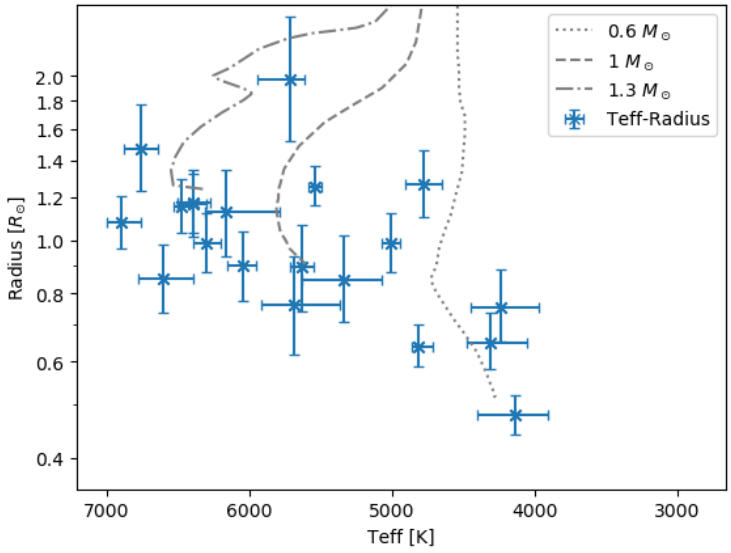

(a) Plot of radius against temperature of the main-sequence companion in the composite systems.

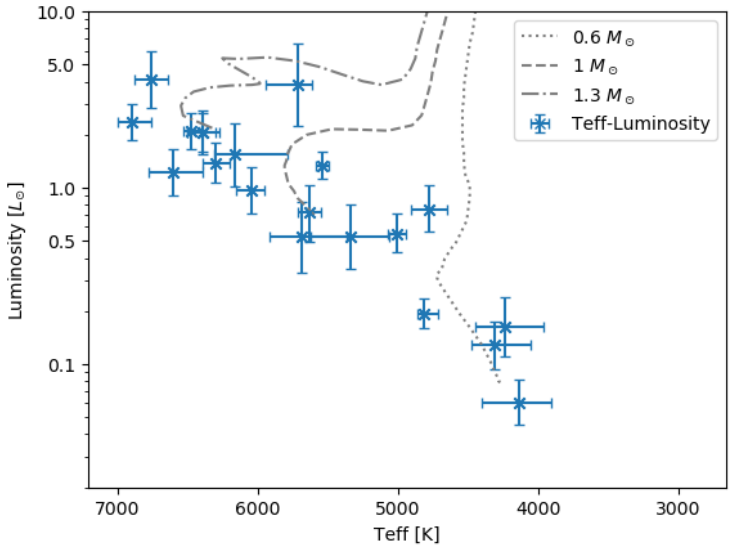

(b) Plot of luminosity against temperature of the main-sequence companion in the composite systems.

Figure 29: Plots for the stellar parameters of the main-sequence companions to the hot subdwarfs in composite systems. The upper panel shows the radius-temperature plot. The lower panel shows the luminosity-temperature plot. Theoretical evolutionary models from Girardi et al. (2000) for solar metallicity are plotted as well for stars with initial masses of 0.6 $M_\odot$, 1 $M_\odot$ and 1.3 $M_\odot$. The evolutionary start of the zero-age main-sequence lies at the smallest radius/luminosity respectively.

4. Conclusion and Outlook

I analyzed the content of the spectroscopic follow-up to the hot subdwarfs found in the Hamburg Quasar Survey. Specifically the spectra for the stars in Edelmann et al. (2003), which consist mostly of sdB and sdOB stars. From these spectra the atmospheric parameters temperature, surface gravity and helium abundance were derived. Furthermore, spectral energy distribution fits were performed for these stars by using measurements from many catalogs of photometric surveys covering the spectrum from the UV (GALEX), the optical and the infrared (e.g. 2MASS). By combining the results from the spectroscopic analyis and the photometric analysis with the parallaxes measured by the Gaia space satellite the stellar parameters mass, radius and luminosity for the stars in the sample could be derived. The conclusions from these results can be summarized as:

- The atmospheric parameters are improved upon the results from Edelmann et al. (2003) by using new detailed model atmospheres and a global spectroscopic fitting method which was used on all hot subdwarfs as the new model includes metal line blanketing and NLTE effects. This improvement in atmospheric parameters is especially important for hot subdwarfs with temperatures above 30 000 K.

- The atmospheric parameters can be analyzed in the Kiel-diagram where the surface gravity is plotted against the temperature. Here the stars from the sample show groupings which are in agreement with predictions made from theoretical evolutionary models. There are four groups of hot subdwarfs to be found in the Kiel-diagram: The cooler sdBs with $T_{\mathrm{eff}} < 25\,000\,\mathrm{K}$ are separated from the other sdBs with higher temperatures. sdOBs and some low-gravity sdBs that are already evolved beyond the EHB.

- The helium abundance of sdB stars seems to be correlated with the effective temperature of the star. This observation is also made in other hot subdwarf surveys like Edelmann et al. (2003) as well as from the Arizona-Montreal Spectroscopic Program in Fontaine et al. (2014) .

- Independent spectra for the stars from this sample were gathered from the SDSS and LAMOST surveys and analysed to gain atmospheric parameters. The comparison between the results from the spectra of the spectroscopic follow-up to the HQS survey and the SDSS/LAMOST spectra show no systematic differences.

- By using the measurements from photometric surveys across the spectral wavelengths from the UV over the optical to the infrared and fitting synthetic

flux distributions that are based on the new model atmospheres composite system for the stars in this sample can be identified and characterized. By doing this the composite spectrum subdwarfs from Edelmann et al. (2003) are confirmed. In addition three new systems (HS0232+3155, HS1824+5745 and HS2151+0857) are identified to be composite.

- Stellar parameters were determined for the stars in this sample by fitting the SEDs with the atmospheric parameters fixed from the spectral analysis. The SED fit determines the angular diameter Θ and the colour excess E(44-55) of the star and by combining this with the parallaxes ϖ determined by the Gaia mission the stellar parameters are calculated. The radius comes from the angular diameter and the parallax, the luminosity from the radius and the effective temperature and the mass from the radius and the surface gravity.

- The radii of the non-composite stars show a distribution in the radius-temperature plane that is also well described by canonical evolutionary models and from the fits we can say that the radii for the sdB and sdOBs from the HQS survey lie in the range from $R = 0.1\,\mathrm{R}_\odot$ to $R = 0.3\,\mathrm{R}_\odot$.

- The luminosities of the non-composite stars in the sample also align well with canonical evolutionary models in the luminosity-temperature plane. Most of the hot subdwarfs in this sample have luminosities in the range of $L = 10\,\mathrm{L}_\odot$ to $L = 30\,\mathrm{L}_\odot$.

- The canonical mass of sdB stars is $M = 0.47\,\mathrm{M}_\odot$ which comes from them being helium-burning stars that are the stripped core of red giants. But measurements of the mass of hot subdwarfs can only now become possible for larger samples as higher precision parallaxes from the Gaia satellite open the door for these mass measurements. The median of the mass distribution found in this sample is found to be $0.433\,\mathrm{M}_\odot$, which is in good agreement with other investigations using the SED + parallax method like V. Schaffenroth et al. (2022) and the theoretical binary population synthesis models (Han et al., 2003).

- The temperatures, radii and luminosities of the companions to the hot subdwarfs that are derived from the SED fitting and single-model spectra fits are consistent with those main-sequence stars that belong to the F, G, K or M spectral type. The radii and luminosities of the hot component of the composite systems show a similar temperature distribution to the non-composite.

The determination of stellar parameters of hot subdwarfs requires both good spectroscopic measurements and photometric coverage. Due to the advancement of stellar parallax measurements with Gaia the feasibility of studies on stellar parameters is made possible for the first time.

In the near future there will also be an advancement in available spectroscopic measurements. The ESO instrument 4MOST (De Jong et al. (2019)), which stands for 4-meter Multi-Object Spectroscopic Telescope will be a spectrograph on the 4m-VISTA telescope dedicated to obtaining spectra of faint objects. With its large field of view of 4.2 square degrees it can take about 2400 spectra simultaneously through optical fibers and survey a large part of the southern sky. A part of these observed objects will also be hot subdwarfs which will allow detailed determinations of stellar parameters and metallicities. The instrument is supposed to start observation in Q1 2025 ESO (2024).

The spectroscopic analysis of composite systems in this work was restricted to single-model spectra fits. To gain a better determination of especially surface gravities and inherently the masses of the components two models, one for the hot subdwarf and one for the companion, need to be combined and fitted to the spectra. Aiming for their mass distribution could be grounds for future works.
The study of stellar parameters of hot subdwarfs will allow for a better understanding of their origin and the nature of binary evolution of stars.

References

Abdurro'uf, None et al. (2022). "The seventeenth data release of the Sloan Digital Sky Surveys: Complete release of MaNGA, MaStar, and APOGEE-2 data". In: *The Astrophysical Journal. Supplement Series* 259.2.

Ashman, Keith M and Stephen E Zepf (2008). *Globular cluster systems*. Cambridge University Press.

Blanton, Michael R et al. (2017). "Sloan digital sky survey IV: Mapping the Milky Way, nearby galaxies, and the distant universe". In: *The Astronomical Journal* 154.1, p. 28.

Crivellari, Lucio, Sergio Simón-Díaz, and María Jesús Arévalo (2020). *Radiative Transfer in Stellar and Planetary Atmospheres*. Vol. 29. Cambridge University Press.

Cui, Xiang-Qun et al. (2012). "The large sky area multi-object fiber spectroscopic telescope (LAMOST)". In: *Research in Astronomy and Astrophysics* 12.9, p. 1197.

Culpan, Richard et al. (2024). "Probing the inner Galactic Halo with blue horizontal branch stars: Gaia DR3 based catalogue with atmospheric and stellar parameters". In: *arXiv preprint arXiv:2402.09779*.

De Jong, Roelof S et al. (2019). "4MOST: Project overview and information for the First Call for Proposals". In: *arXiv preprint arXiv:1903.02464*.

Dorman, Ben, Robert T Rood, and Robert W O'Connell (1993). "Ultraviolet Radiation from Evolved Stellar Populations. I. Models". In: *Astrophysical Journal v. 419, p. 596* 419, p. 596.

Edelmann, Heinz et al. (2003). "Spectral analysis of sdB stars from the Hamburg Quasar Survey". In: *Astronomy & Astrophysics* 400.3, pp. 939–950.

ESA (2013). *The Gaia Mission*. [Online; last accessed 7-April-2024]. URL: https://www.cosmos.esa.int/web/gaia/the-mission.

ESO (2024). *4MOST - 4-metre Multi-Object Spectroscopic Telescope*. [Online; last accessed 5-April-2024]. URL: https://www.eso.org/sci/facilities/develop/instruments/4MOST.html.

Fitzpatrick, Edward L (1999). "Correcting for the effects of interstellar extinction". In: *Publications of the Astronomical Society of the Pacific* 111.755, p. 63.

Fitzpatrick, Edward L et al. (2019). "An analysis of the shapes of interstellar extinction curves. VII. Milky Way spectrophotometric optical-through-ultraviolet extinction and its R-dependence". In: *The Astrophysical Journal* 886.2, p. 108.

Fontaine, G et al. (2014). "Results from the Arizona-Montréal Spectroscopic Program: A Detailed Look at the He Abundance Pattern in Hot Subdwarfs". In: *6th Meeting on Hot Subdwarf Stars and Related Objects*. Vol. 481, p. 83.

Giddings, J. R. (1981). "Quantum Particles in Kerr-Newman Fields". PhD thesis. University of London.

Girardi, Léo et al. (2000). "Evolutionary tracks and isochrones for low-and intermediate-mass stars: From 0.15 to 7, and from to 0.03". In: *Astronomy and Astrophysics Supplement Series* 141.3, pp. 371–383.

Girven, Jonathan et al. (2012). "The unseen population of F-to K-type companions to hot subdwarf stars". In: *Monthly Notices of the Royal Astronomical Society* 425.2, pp. 1013–1041.

Graser, U. (1998). *Cassegrain TWIN Spectrograph 3.5 m Telescope Calar Alto User´s Manual*. [Online; last accessed 7-April-2024]. URL: https://www.caha.es/CAHA/Instruments/TWIN/HTML/twin.html#developments.

Gray, David F (2021). *The observation and analysis of stellar photospheres*. Cambridge university press.

Hagen, H-J et al. (1995). "The Hamburg Quasar Survey. I. Schmidt observations and plate digitization." In: *Astronomy and Astrophysics Supplement, v. 111, p. 195* 111, p. 195.

Han, Zhan-wen et al. (2003). "The origin of subdwarf B stars–II". In: *Monthly Notices of the Royal Astronomical Society* 341.2, pp. 669–691.

Heber, Ulrich (2009). "Hot subdwarf stars". In: *Annual review of Astronomy and Astrophysics* 47, pp. 211–251.

— (2016a). "Hot subluminous stars". In: *Publications of the Astronomical Society of the Pacific* 128.966, p. 082001.

— (2016b). "Stripped red giants-Helium core white dwarf progenitors and their sdB siblings". In: *arXiv preprint arXiv:1610.07516*.

Heber, Ulrich, Andreas Irrgang, and Johannes Schaffenroth (2018). "Spectral energy distributions and colours of hot subluminous stars". In: *Open Astronomy* 27.1, pp. 35–43.

Houck, JC and LA Denicola (2000). "ISIS: An interactive spectral interpretation system for high resolution X-ray spectroscopy". In: *Astronomical Data Analysis Software and Systems IX*. Vol. 216, p. 591.

Husser, T-O et al. (2013). "A new extensive library of PHOENIX stellar atmospheres and synthetic spectra". In: *Astronomy & Astrophysics* 553, A6.

Irrgang, Andreas, Simon Kreuzer, et al. (2018). "A quantitative spectral analysis of 14 hypervelocity stars from the MMT survey". In: *Astronomy & Astrophysics* 615, p. L5.

Irrgang, Andreas, Norbert Przybilla, et al. (2014). "A new method for an objective, χ2-based spectroscopic analysis of early-type stars-First results from its application to single and binary B-and late O-type stars". In: *Astronomy & Astrophysics* 565, A63.

Kurucz, Robert L (1996). "Status of the ATLAS 12 Opacity Sampling Program and of New Programs for Rosseland and for Distribution Function Opacity". In: *MASS; Model Atmospheres and Spectrum SynthesisASP Conference Series;*

Vol. 108; 1996; ed. Saul J. Adelman; Friedrich Kupka; and Warner W. Weiss (1996), p. 160. Vol. 108, p. 160.

Martin, D Christopher et al. (2005). "The Galaxy Evolution Explorer: a space ultraviolet survey mission". In: *The Astrophysical Journal* 619.1, p. L1.

Moehler, Sabine et al. (2014). "Flux calibration of medium-resolution spectra from 300 nm to 2500 nm: Model reference spectra and telluric correction". In: *Astronomy & Astrophysics* 568, A9.

Owocki, Stan (2021). *Fundamentals of astrophysics*. Cambridge University Press.

Paczynski, B (1971). "Evolution of single stars. IV. Helium stars". In: *Acta Astronomica, Vol. 21, p. 1* 21, p. 1.

Padmanabhan, Thanu (2000). *Theoretical astrophysics: volume 2, stars and stellar systems*. Cambridge University Press.

Papageorgiou, Athanasios et al. (2018). "An updated catalog of 4680 northern eclipsing binaries with Algol-type light-curve morphology in the Catalina sky surveys". In: *The Astrophysical Journal Supplement Series* 238.1, p. 4.

Prusti, Timo et al. (2016). "The gaia mission". In: *Astronomy & astrophysics* 595, A1.

Schaffenroth, Veronika et al. (2022). "Hot subdwarfs in close binaries observed from space-I. Orbital, atmospheric, and absolute parameters, and the nature of their companions". In: *Astronomy & Astrophysics* 666, A182.

Schaller, G et al. (1992). "New grids of stellar models from 0.8 to 120 solar masses at Z= 0.020 and Z= 0.001". In: *Astronomy and Astrophysics Supplement Series (ISSN 0365-0138), vol. 96, no. 2, p. 269-331.* 96, pp. 269–331.

Vallenari, Antonella et al. (2023). "Gaia data release 3-summary of the content and survey properties". In: *Astronomy & Astrophysics* 674, A1.

A. Tables for spectroscopic and photometric fits

Table 1: Table of the spectroscopic fit parameters for the stars from the spectroscopic follow-up to the HQS survey. The spectrum of HS0231+8019 could not be fitted due to a problem with the wavelength calibration. HS1556+6032 was classified as a main-sequence B star in Edelmann et al. (2003), the stellar parameters make this unlikely (see 3.2.2)

Name	Class	Resolution [Å]	$T_{\rm eff}$ [K]	$\log g$ [dex]	$\log$ He [dex]
HS0016+0044	binary	5.0	27300 ± 1100	5.08 ± 0.14	$-2.91^{+0.11}_{-0.1}$
HS0023+3049	sdB	5.0	31800 ± 1200	5.88 ± 0.13	$-3.8^{+0.5}_{-0.7}$
HS0025+3423	sdOB	3.4	32900 ± 1100	6.02 ± 0.11	-0.947 ± 0.022
HS0028+4408	binary	6.0	34500 ± 1400	5.23 ± 0.12	$-1.92^{+0.08}_{-0.1}$
HS0035+3034	sdOB	3.4	38400 ± 1300	5.97 ± 0.12	$-1.526^{+0.029}_{-0.03}$
HS0039+4302	sdB	6.0	32300 ± 1000	5.78 ± 0.11	-2.28 ± 0.05
HS0040+4417	sdB	7.0	30300 ± 1200	5.62 ± 0.15	$-1.78^{+0.11}_{-0.12}$
HS0048+0026	sdOB	5.0	38000 ± 1200	5.61 ± 0.11	-1.13 ± 0.04
HS0055+0138	sdB	5.0	33000 ± 1100	5.62 ± 0.12	$-1.97^{+0.04}_{-0.05}$
HS0127+3146	binary	6.0	37400 ± 1200	5.25 ± 0.11	-3.23 ± 0.17
HS0136+0605	binary	7.0	19700 ± 900	5.81 ± 0.15	$-3.1^{+0.4}_{-0.5}$
HS0209+0141	sdB	5.0	30200 ± 1000	5.61 ± 0.11	-2.74 ± 0.07
HS0212+1446	sdB	7.0	29100 ± 1100	5.73 ± 0.14	$-3^{+0.14}_{-0.18}$
HS0213+2329	sdOB	3.5	32300 ± 1000	5.5 ± 0.11	$-1.578^{+0.019}_{-0.017}$
HS0215+0852	binary	7.0	43000 ± 5000	5.2 ± 0.4	$-2.91^{+0.29}_{-0.4}$
HS0231+8019	B	-	-	-	-
HS0232+3155	binary	3.5	35900 ± 1200	5.79 ± 0.11	$-4.3^{+0.5}_{-0.8}$
HS0233+3037	sdB	3.5	26800 ± 900	5.66 ± 0.11	-2.6 ± 0.06
HS0252+1025	binary	3.5	42800 ± 1400	5.29 ± 0.11	-2.77 ± 0.08
HS0338+2946	sdB	6.0	30000 ± 1000	5.82 ± 0.11	-2.9 ± 0.08
HS0349+0700	sdB	7.0	26300 ± 1000	5.56 ± 0.15	$-2.68^{+0.1}_{-0.11}$
HS0352+1019	sdB	6.0	26100 ± 800	5.55 ± 0.11	-2.93 ± 0.05
HS0357+0133	sdB	3.4	29200 ± 1000	5.74 ± 0.11	-2.82 ± 0.1
HS0430+7712	sdB	6.0	26600 ± 800	5.5 ± 0.11	$-3.08^{+0.05}_{-0.09}$
HS0444+0458	sdB	5.0	31700 ± 1400	5.52 ± 0.16	-1.9 ± 0.09
HS0445+7503	sdB	6.0	31100 ± 1000	5.79 ± 0.11	$-2.048^{+0.02}_{-0.04}$
HS0446+1344	binary	6.0	50300 ± 1600	5.62 ± 0.11	-3.34 ± 0.09
HS0447+7545	sdB	6.0	30400 ± 1000	5.58 ± 0.11	-2.29 ± 0.1
HS0457+0907	sdOB	6.0	37300 ± 1200	5.75 ± 0.11	$-1.55^{+0.02}_{-0.05}$

HS0546+8009	sdOB	3.5	35100 ± 1100	5.85 ± 0.11	$-1.994^{+0.019}_{-0.02}$
HS0600+6602	sdOB	5.0	35800 ± 1200	5.92 ± 0.14	-1.43 ± 0.05
HS0656+6117	binary	5.5	30900 ± 2200	4.94 ± 0.22	$-2.3^{+0.12}_{-0.14}$
HS0702+6043	sdB	7.0	29700 ± 1300	5.82 ± 0.17	$-2.64^{+0.13}_{-0.21}$
HS0705+6700	sdB	6.5	27600 ± 1200	5.45 ± 0.16	$-2.59^{+0.1}_{-0.16}$
HS0707+8225	sdB	5.0	27800 ± 900	5.44 ± 0.11	$-3.55^{+0.19}_{-0.4}$
HS0740+3734	sdB	5.0	22000 ± 700	5.27 ± 0.11	$-2.258^{+0.03}_{-0.04}$
HS0741+3818	sdB	5.0	31300 ± 1100	5.35 ± 0.12	-1.43 ± 0.04
HS0815+4243	sdOB	3.5	34200 ± 1100	6.01 ± 0.11	$-2.08^{+0.03}_{-0.04}$
HS0941+4649	sdB	5.0	32900 ± 1300	4.87 ± 0.13	-2.23 ± 0.23
HS0942+4608	binary	5.0	32000 ± 1500	5.16 ± 0.19	-1.92 ± 0.08
HS1051+2933	sdOB	3.5	36600 ± 1200	5.96 ± 0.11	-0.75 ± 0.016
HS1106+6051	binary	5.0	34000 ± 1200	4.91 ± 0.13	-1.88 ± 0.07
HS1236+4754	sdB	5.0	27000 ± 900	5.5 ± 0.12	$-2.54^{+0.07}_{-0.12}$
HS1320+2622	sdB	3.5	28500 ± 900	5.63 ± 0.11	$-2.71^{+0.09}_{-0.1}$
HS1511+6221	binary	5.0	50600 ± 1900	5.48 ± 0.11	$-3.55^{+0.16}_{-0.22}$
HS1547+6312	sdB	5.5	32200 ± 1300	5.81 ± 0.16	$-3.8^{+0.5}_{-1.3}$
HS1552+6333	sdB	5.5	34700 ± 1200	5.72 ± 0.12	$-2.03^{+0.07}_{-0.09}$
HS1556+6032	B?	5.5	12600 ± 400	3.7 ± 0.11	$-1.25^{+0.028}_{-5e-16}$
HS1612+6337	binary	5.5	6550 ± 200	3.8 ± 0.12	-1 ± 0
HS1612+7335	binary	5.5	32600 ± 1400	4.65 ± 0.15	$-1.87^{+0.09}_{-0.11}$
HS1615+6341	binary	5.5	25800 ± 1100	4.6 ± 0.19	$-1.9^{+0.14}_{-0.15}$
HS1641+4601	sdB	1.5	30100 ± 1000	5.69 ± 0.11	-1.755 ± 0.03
HS1717+6042	sdB	5.0	29100 ± 1000	5.58 ± 0.11	-2.45 ± 0.04
HS1736+8001	sdB	5.5	29200 ± 1000	4.87 ± 0.11	$-5^{+0.4}_{-8e-08}$
HS1739+5244	sdB	3.5	39500 ± 1300	5.71 ± 0.11	$-3.89^{+0.3}_{-0.4}$
HS1741+2133	sdOB	3.6	38600 ± 1200	5.54 ± 0.11	$-2.494^{+0.027}_{-0.026}$
HS1747+6924	sdB	5.0	27300 ± 900	5.57 ± 0.11	$-3.08^{+0.14}_{-0.18}$
HS1747+8013	sdB	5.5	30600 ± 2000	5.51 ± 0.24	$-2.71^{+0.23}_{-0.26}$
HS1753+5342	binary	3.6	41400 ± 1700	4.98 ± 0.14	-2.4 ± 0.08
HS1753+7025	binary	5.5	24600 ± 800	4.66 ± 0.11	$-3.6^{+0.4}_{-0.27}$
HS1756+7056	sdB	5.5	28800 ± 1000	5.62 ± 0.11	$-3.36^{+0.22}_{-0.23}$
HS1806+5024	sdOB	3.5	36600 ± 1200	5.62 ± 0.11	-1.476 ± 0.022
HS1813+7247	sdB	5.5	25700 ± 1000	5.17 ± 0.13	$-2.59^{+0.1}_{-0.12}$
HS1824+5745	binary	5.0	33500 ± 1400	6.1 ± 0.16	$-1.69^{+0.11}_{-0.1}$
HS1831+6432	sdOB	5.0	37600 ± 1200	5.93 ± 0.11	$-1.598^{+0.029}_{-0.04}$
HS1831+7647	sdB	6.0	22600 ± 700	5.37 ± 0.1	-2.97 ± 0.06
HS1832+7009	sdB	5.5	27500 ± 900	5.52 ± 0.11	$-1.857^{+0.014}_{-0.016}$
HS1839+7951	sdB	5.5	23300 ± 3000	5.2 ± 0.4	$-2.72^{+0.27}_{-0.25}$
HS1842+6557	sdB	5.0	37300 ± 1900	6.5 ± 0.29	$-1.23^{+0.16}_{-0.17}$

HS1843+6953	sdB	8.0	41500 ± 1500	5.64 ± 0.12	$-3.3^{+0.4}_{-0.6}$
HS1844+5048	binary	3.5	56900 ± 2200	5.84 ± 0.12	-1.99 ± 0.06
HS1846+8149	sdB	6.0	25900 ± 800	5.5 ± 0.11	-2.77 ± 0.06
HS1858+5736	binary	5.0	34500 ± 1300	5.46 ± 0.12	$-5^{+0.5}_{-2.8e-11}$
HS1859+6219	sdB	5.0	26800 ± 900	5.33 ± 0.12	$-2.47^{+0.06}_{-0.05}$
HS1917+7009	sdB	3.6	26900 ± 900	5.41 ± 0.11	$-3.01^{+0.04}_{-0.07}$
HS1926+6946	sdB	5.5	22600 ± 1300	4.91 ± 0.16	-2.85 ± 0.12
HS2005+7933	sdB	3.6	24900 ± 1000	5.15 ± 0.13	-2.97 ± 0.05
HS2028+0107	sdOB	5.0	34700 ± 1300	5.74 ± 0.16	-1.52 ± 0.04
HS2029+0301	sdB	5.0	30900 ± 1000	5.78 ± 0.11	$-2.19^{+0.05}_{-0.06}$
HS2033+0507	sdB	3.4	27200 ± 900	5.42 ± 0.11	$-2.4^{+0.09}_{-0.08}$
HS2035+0418	sdB	5.0	27400 ± 900	5.44 ± 0.11	-2.49 ± 0.05
HS2100+1710	sdOB	3.4	34400 ± 1200	5.89 ± 0.14	$-1.61^{+0.09}_{-0.1}$
HS2100+1710 Run 2	sdOB	5.0	35300 ± 1100	5.85 ± 0.11	$-1.452^{+0.013}_{-0.014}$
HS2126+8320	sdB	5.5	23700 ± 1200	5.02 ± 0.16	$-2.95^{+0.11}_{-0.12}$
HS2126+8320 Run 2	sdB	6.0	27200 ± 900	5.44 ± 0.11	-2.83 ± 0.05
HS2131+0349	B	5.0	13000 ± 400	3.44 ± 0.11	$-1.07^{+0.04}_{-0.05}$
HS2143+8157	sdB	5.5	25900 ± 1000	5.15 ± 0.13	$-2.61^{+0.09}_{-0.11}$
HS2149+0847	sdOB	5.0	36900 ± 1400	6.11 ± 0.16	-1.85 ± 0.1
HS2149+1428	sdB	7.0	36400 ± 1600	5.71 ± 0.15	$-3.5^{+0.5}_{-1.6}$
HS2151+0214	sdB	5.0	31000 ± 1000	5.76 ± 0.11	-2.35 ± 0.08
HS2151+0857	binary	5.0	34200 ± 1700	5.96 ± 0.22	$-1.48^{+0.1}_{-0.11}$
HS2156+2215	sdOB	3.6	35500 ± 1200	5.47 ± 0.11	$-2.99^{+0.07}_{-0.05}$
HS2156+2517	sdB	7.0	36600 ± 1200	6.14 ± 0.11	$-5^{+0.8}_{-1.3e-11}$
HS2158+2137	sdB	6.0	31500 ± 1000	5.87 ± 0.11	-2.22 ± 0.04
HS2201+2610	sdB	3.5	28700 ± 900	5.57 ± 0.11	$-3.07^{+0.07}_{-0.08}$
HS2206+2847	sdB	3.5	31500 ± 1000	5.83 ± 0.11	-1.818 ± 0.026
HS2208+2718	sdB	3.5	28800 ± 900	5.59 ± 0.11	$-5.05^{+1.6}_{-0}$
HS2209+2840	sdB	3.5	29900 ± 1000	5.79 ± 0.11	$-1.806^{+0.026}_{-0.024}$
HS2213+1336	sdB	5.5	19900 ± 800	4.81 ± 0.12	$-2.12^{+0.08}_{-0.09}$
HS2216+1833	binary	3.6	32600 ± 1300	4.99 ± 0.15	-1.92 ± 0.04
HS2218+0201	sdB	5.0	24800 ± 800	5.27 ± 0.11	-2.81 ± 0.08
HS2224+2618	sdB	7.0	20800 ± 700	4.76 ± 0.11	$-1.908^{+0.028}_{-0.02}$
HS2225+2220	sdB	3.5	30700 ± 1000	5.84 ± 0.11	-1.82 ± 0.04
HS2229+0910	sdOB	7.0	38100 ± 1300	6.21 ± 0.12	-1.82 ± 0.05
HS2229+2628	HBB	8.0	19600 ± 800	4.47 ± 0.14	$-1.89^{+0.1}_{-0.08}$
HS2231+2441	sdB	6.0	28000 ± 900	5.56 ± 0.11	-3.27 ± 0.13
HS2233+1418	sdOB	7.0	39100 ± 1400	5.76 ± 0.13	$-2.59^{+0.11}_{-0.14}$
HS2233+2332	sdB	3.5	26800 ± 900	5.43 ± 0.11	-2.95 ± 0.06
HS2233+2332 Run 2	sdB	5.0	25000 ± 800	5.27 ± 0.11	-2.91 ± 0.04

HS2240+0136	sdB	3.4	31000 ± 1000	5.94 ± 0.11	-2.35 ± 0.05
HS2240+1031	sdOB	5.5	34400 ± 1100	5.61 ± 0.11	-1.56 ± 0.04
HS2242+3206	sdB	3.5	28600 ± 900	5.74 ± 0.11	-3.1 ± 0.05
HS2246+0158	sdB	5.0	34200 ± 1200	5.8 ± 0.13	-1.71 ± 0.08
HS2333+3927	sdOB	3.4	39600 ± 1300	5.89 ± 0.11	-2.39 ± 0.05
HS2333+3927 Run 2	sdOB	5.0	42800 ± 1400	5.81 ± 0.11	$-2.61^{+0.15}_{-0.06}$

Table 2: Table of the spectroscopic fit parameters for the spectra from the SDSS and LAMOST surveys. Here the statistical uncertainties are given.

Name	$T_{\rm eff}$ [K]	$\log g$ [dex]	$\log$ He [dex]
SDSS			
HS0016+0044	28200^{+70}_{-60}	$5.402^{+0.01}_{-0.009}$	-2.9 ± 0.04
HS0048+0026 Run 1	34200^{+600}_{-700}	6.31 ± 0.11	-1.47 ± 0.07
HS0048+0026 Run 2	38190^{+80}_{-110}	$5.917^{+0.018}_{-0.014}$	$-1.147^{+0.015}_{-0.013}$
HS0048+0026 Run 3	38030^{+80}_{-100}	$5.96^{+0.013}_{-0.014}$	-1.131 ± 0.013
HS0815+4243 Run 1	33640^{+170}_{-130}	$5.892^{+0.021}_{-0.027}$	-2.1 ± 0.05
HS0815+4243 Run 2	34410^{+180}_{-100}	$5.997^{+0.022}_{-0.027}$	-2.15 ± 0.04
HS0815+4243 Run 3	34070^{+90}_{-130}	5.94 ± 0.016	$-2.06^{+0.04}_{-0.05}$
HS0941+4649	34100^{+400}_{-170}	$5.078^{+0.027}_{-0.023}$	$-2.57^{+0.07}_{-0.09}$
HS1051+2933 Run 1	37300^{+130}_{-220}	$6.023^{+0.024}_{-0.021}$	$-0.75^{+0.014}_{-0.008}$
HS1051+2933 Run 2	37220^{+210}_{-220}	5.87 ± 0.04	$-0.75^{+0.017}_{-0.014}$
HS1051+2933 Run 3	37030^{+160}_{-170}	$5.949^{+0.026}_{-0.025}$	-0.722 ± 0.015
HS1236+4754	27600 ± 130	$5.555^{+0.024}_{-0.021}$	$-2.56^{+0.04}_{-0.05}$
HS1831+6432	37520 ± 100	$6^{+0.013}_{-0.014}$	-1.629 ± 0.017
HS2213+1336	21310^{+60}_{-110}	4.951 ± 0.011	-2.137 ± 0.024
HS2225+2220 Run 1	31580^{+50}_{-40}	$5.901^{+0.008}_{-0.006}$	-2.18 ± 0.04
HS2225+2220 Run 2	31630^{+80}_{-90}	5.796 ± 0.012	-2.095 ± 0.029
LAMOST			
HS0016+0044	27960^{+80}_{-70}	5.305 ± 0.01	-3.45 ± 0.06
HS0023+3049	29000 ± 50	$5.552^{+0.007}_{-0.008}$	$-5^{+0.5}_{-0.06}$
HS0025+3423 Run 1	33380^{+110}_{-90}	$5.857^{+0.011}_{-0.019}$	-0.931 ± 0.01
HS0025+3423 Run 2	33900^{+500}_{-700}	$5.77^{+0.07}_{-0.08}$	$-0.92^{+0.05}_{-0.04}$

HS0055+0138	33100^{+400}_{-500}	$5.76^{+0.06}_{-0.05}$	$-1.904^{+0.03}_{-0.04}$
HS0127+3146 Run 1	32300^{+1100}_{-1400}	$4.6^{+0.07}_{-0}$	$-2.27^{+0.22}_{-0.2}$
HS0127+3146 Run 2	34400^{+1900}_{-1800}	$5.39^{+0.28}_{-0.25}$	$-2.22^{+0.26}_{-0.23}$
HS0127+3146 Run 3	35500 ± 500	5.12 ± 0.05	$-2.7^{+0.12}_{-0.13}$
HS0209+0141	30430^{+190}_{-210}	$5.672^{+0.023}_{-0.021}$	-2.79 ± 0.06
HS0233+3037 Run 1	26620 ± 60	$5.554^{+0.009}_{-0.011}$	-2.486 ± 0.022
HS0233+3037 Run 2	23000^{+900}_{-800}	$5.27^{+0.12}_{-0.11}$	$-2.51^{+0.07}_{-0.08}$
HS0352+1019	25440^{+130}_{-120}	$5.338^{+0.02}_{-0.016}$	$-2.78^{+0.05}_{-0.04}$
HS0357+0133 Run 1	28530^{+290}_{-400}	$5.6^{+0.029}_{-0.026}$	-2.36 ± 0.07
HS0357+0133 Run 2	27900 ± 400	$5.492^{+0.03}_{-0.04}$	-2.41 ± 0.07
HS0600+6602	34100^{+1000}_{-1200}	$5.96^{+0.18}_{-0.16}$	-1.17 ± 0.11
HS0741+3818	28020^{+110}_{-90}	5.297 ± 0.015	-0.984 ± 0.011
HS0815+4243	33500 ± 400	5.86 ± 0.06	-2.1 ± 0.07
HS0941+4649 Run 1	34700^{+700}_{-800}	$5.18^{+0.06}_{-0.09}$	-2.48 ± 0.09
HS0941+4649 Run 2	33200^{+1300}_{-1000}	$4.75^{+0.13}_{-0.08}$	$-2.55^{+0.21}_{-0.27}$
HS1051+2933 Run 1	37300^{+400}_{-600}	6.07 ± 0.09	$-0.72^{+0.04}_{-0.05}$
HS1051+2933 Run 2	36600 ± 400	5.93 ± 0.06	-0.727 ± 0.028
HS1236+4754	28400^{+400}_{-500}	5.64 ± 0.06	$-2.37^{+0.07}_{-0.08}$
HS1741+2133	39300^{+400}_{-280}	$5.63^{+0.05}_{-0.04}$	-2.43 ± 0.08
HS1753+5342	49000^{+5000}_{-4000}	$4.84^{+0.24}_{-0.12}$	$-2.43^{+0.14}_{-0.29}$
HS1858+5736	30800^{+400}_{-300}	5.11 ± 0.04	$-4.07^{+0.29}_{-0.5}$
HS2131+0349	12500 ± 500	$3.4^{+0.15}_{-0.16}$	$-1^{+0}_{-0.06}$
HS2158+2137	33500^{+1000}_{-1100}	$5.8^{+0.11}_{-0.16}$	$-2.17^{+0.18}_{-0.21}$
HS2213+1336	21070^{+160}_{-170}	$4.79^{+0.08}_{-0.023}$	$-2.17^{+0.04}_{-0.06}$
HS2216+1833	33300^{+900}_{-500}	$5.02^{+0.1}_{-0.07}$	-1.63 ± 0.06
HS2231+2441	27860^{+70}_{-90}	$5.496^{+0.009}_{-0.015}$	$-2.85^{+0.04}_{-0.05}$
HS2233+1418 Run 1	32600^{+1800}_{-2200}	$5^{+0.18}_{-0.21}$	$-2.48^{+0.23}_{-0.3}$
HS2233+1418 Run 2	35470^{+190}_{-200}	$5.168^{+0.02}_{-0.021}$	$-2.51^{+0.05}_{-0.06}$
HS2240+0136	30120^{+70}_{-60}	5.953 ± 0.01	-2.355 ± 0.022
HS2240+1031	35040^{+100}_{-90}	5.83 ± 0.015	$-1.55^{+0.009}_{-0.012}$
HS2242+3206	29680 ± 50	$5.674^{+0.007}_{-0.008}$	-2.831 ± 0.03

Table 3: Table of parameters from the photometric fits. Listed are the mass M, radius R and luminosity L of the star as well as their colour excess E(44-55), parallax $\overline{\omega}$ and angular diameter $\log\Theta$.

Name	Class	M $[M_\odot]$	R $[R_\odot]$	L $[L_\odot]$	E(44-55) [mag]	$\overline{\omega}$ [mas]	$\log\Theta$ [dex]
HS0016+0044	binary	$0.2^{+0.09}_{-0.07}$	$0.215^{+0.021}_{-0.018}$	23^{+7}_{-5}	$0^{+0.009}_{-0}$	0.65 ± 0.05	$-11.206^{+0.021}_{-0.015}$
HS0023+3049	sdB	$0.8^{+0.29}_{-0.22}$	$0.17^{+0.013}_{-0.011}$	27^{+6}_{-5}	$0^{+0}_{-0.0006}$	0.85 ± 0.04	$-11.183^{+0.015}_{-0.014}$
HS0025+3423	sdOB	$0.5^{+0.16}_{-0.13}$	$0.115^{+0.009}_{-0.008}$	$13.9^{+2.8}_{-2.3}$	$0.098^{+0.003}_{-0.008}$	0.81 ± 0.08	$-11.376^{+0.01}_{-0.012}$
HS0028+4408	binary	$0.33^{+0.24}_{-0.13}$	$0.23^{+0.07}_{-0.05}$	70^{+50}_{-23}	$0.02^{+0.09}_{-0.02}$	0.3 ± 0.13	$-11.52^{+0.09}_{-0.03}$
HS0035+3034	sdOB	$0.38^{+0.15}_{-0.11}$	$0.105^{+0.01}_{-0.008}$	22^{+6}_{-4}	0.084 ± 0.007	0.65 ± 0.07	-11.51 ± 0.01
HS0039+4302	sdB	$0.41^{+0.13}_{-0.1}$	$0.137^{+0.011}_{-0.009}$	18 ± 4	$0.07^{+0.004}_{-0.008}$	0.77 ± 0.05	$-11.323^{+0.01}_{-0.012}$
HS0040+4417	sdB	$0.32^{+0.16}_{-0.11}$	$0.145^{+0.014}_{-0.013}$	16^{+5}_{-4}	$0.083^{+0.006}_{-0.017}$	0.62 ± 0.07	$-11.391^{+0.012}_{-0.019}$
HS0048+0026	sdOB	$0.23^{+0.09}_{-0.07}$	$0.125^{+0.013}_{-0.011}$	29^{+8}_{-6}	$0.0273^{+0.0024}_{-0.0029}$	0.57 ± 0.06	$-11.496^{+0.011}_{-0.01}$
HS0055+0138	sdB	$0.3^{+0.11}_{-0.08}$	$0.141^{+0.011}_{-0.01}$	21^{+5}_{-4}	0.019 ± 0.004	0.79 ± 0.06	-11.301 ± 0.011
HS0127+3146	binary	$0.5^{+0.25}_{-0.16}$	$0.28^{+0.05}_{-0.04}$	140^{+60}_{-40}	$0^{+0.07}_{-0.004}$	0.46 ± 0.04	$-11.26^{+0.07}_{-0.013}$
HS0136+0605	binary	$0.065^{+0.03}_{-0.021}$	$0.053^{+0.006}_{-0.005}$	$0.37^{+0.12}_{-0.09}$	$0.14^{+0.04}_{-0.011}$	0.563 ± 0.023	$-11.875^{+0.011}_{-0.009}$
HS0209+0141	sdB	$0.3^{+0.09}_{-0.07}$	$0.142^{+0.007}_{-0.006}$	$15^{+2.4}_{-2.1}$	$0.0344^{+0.0019}_{-0.0025}$	1.35 ± 0.05	-11.066 ± 0.01
HS0212+1446	sdB	$0.74^{+0.3}_{-0.21}$	$0.194^{+0.013}_{-0.012}$	24^{+6}_{-5}	$0^{+0}_{-0.0007}$	0.98 ± 0.04	$-11.066^{+0.016}_{-0.015}$
HS0213+2329	sdOB	$0.49^{+0.15}_{-0.11}$	$0.206^{+0.012}_{-0.011}$	41^{+8}_{-7}	0.106 ± 0.01	1.1 ± 0.05	-10.993 ± 0.011
HS0215+0852	binary	$0.09^{+0.11}_{-0.05}$	$0.119^{+0.015}_{-0.013}$	45^{+24}_{-17}	$0^{+0}_{-0.015}$	0.64 ± 0.04	-11.47 ± 0.04
HS0231+8019	B	-	-	-	-	-	-
HS0232+3155	binary	$0.37^{+0.12}_{-0.09}$	$0.128^{+0.009}_{-0.008}$	24^{+5}_{-4}	$0.167^{+0.012}_{-0.014}$	0.9 ± 0.06	$-11.285^{+0.012}_{-0.014}$
HS0233+3037	sdB	$0.46^{+0.14}_{-0.11}$	0.165 ± 0.007	$12.7^{+2}_{-1.8}$	0.169 ± 0.004	1.64 ± 0.04	-10.914 ± 0.01
HS0252+1025	binary	$0.18^{+0.08}_{-0.06}$	$0.161^{+0.022}_{-0.024}$	78^{+26}_{-22}	$0.24^{+0.06}_{-0.07}$	1.34 ± 0.08	$-11.01^{+0.05}_{-0.07}$
HS0338+2946	sdB	$0.47^{+0.14}_{-0.11}$	0.139 ± 0.007	$14.1^{+2.4}_{-2.1}$	0.242 ± 0.008	1.25 ± 0.05	$-11.106^{+0.011}_{-0.01}$
HS0349+0700	sdB	$0.41^{+0.17}_{-0.12}$	0.175 ± 0.008	$13.2^{+2.4}_{-2.1}$	$0.2071^{+0.0026}_{-0.007}$	1.44 ± 0.04	$-10.943^{+0.011}_{-0.013}$
HS0352+1019	sdB	$0.59^{+0.17}_{-0.13}$	$0.213^{+0.01}_{-0.009}$	$19^{+3}_{-2.7}$	0.2084 ± 0.0024	1.35 ± 0.04	-10.887 ± 0.01
HS0357+0133	sdB	$0.59^{+0.19}_{-0.15}$	$0.172^{+0.009}_{-0.008}$	$19^{+4}_{-2.9}$	0.318 ± 0.005	1.222 ± 0.03	-11.024 ± 0.011
HS0430+7712	sdB	$0.55^{+0.16}_{-0.12}$	$0.218^{+0.01}_{-0.009}$	21^{+4}_{-3}	0.137 ± 0.004	1.418 ± 0.028	-10.855 ± 0.01
HS0444+0458	sdB	$0.29^{+0.15}_{-0.1}$	$0.155^{+0.015}_{-0.013}$	22^{+7}_{-5}	$0.061^{+0.004}_{-0.013}$	0.63 ± 0.06	$-11.356^{+0.014}_{-0.018}$
HS0445+7503	sdB	$0.61^{+0.18}_{-0.14}$	$0.164^{+0.009}_{-0.008}$	23 ± 4	$0.1605^{+0.0026}_{-0.003}$	1.113 ± 0.027	-11.084 ± 0.01
HS0446+1344	binary	$0.55^{+0.21}_{-0.15}$	$0.189^{+0.021}_{-0.019}$	200^{+60}_{-50}	$0.286^{+0.03}_{-0.04}$	0.76 ± 0.05	-11.19 ± 0.04
HS0447+7545	sdB	$0.45^{+0.16}_{-0.12}$	$0.181^{+0.016}_{-0.014}$	25^{+6}_{-5}	0.238 ± 0.011	0.68 ± 0.04	-11.26 ± 0.012
HS0457+0907	sdOB	$0.36^{+0.11}_{-0.08}$	0.132 ± 0.006	30 ± 5	0.1503 ± 0.0024	1.33 ± 0.05	$-11.101^{+0.01}_{-0.009}$
HS0546+8009	sdOB	$0.48^{+0.14}_{-0.11}$	$0.137^{+0.007}_{-0.006}$	26^{+5}_{-4}	$0.0921^{+0.0024}_{-0.004}$	1.281 ± 0.026	-11.102 ± 0.01
HS0600+6602	sdOB	$0.43^{+0.19}_{-0.13}$	$0.12^{+0.012}_{-0.011}$	21^{+6}_{-5}	0.172 ± 0.009	0.58 ± 0.06	$-11.506^{+0.011}_{-0.012}$
HS0656+6117	binary	$0.08^{+0.06}_{-0.04}$	$0.154^{+0.021}_{-0.017}$	20^{+9}_{-6}	$0.099^{+0.014}_{-0.015}$	0.44 ± 0.05	$-11.51^{+0.017}_{-0.019}$
HS0702+6043	sdB	$1.1^{+0.6}_{-0.4}$	$0.211^{+0.018}_{-0.016}$	31^{+8}_{-7}	0.095 ± 0.004	0.71 ± 0.04	$-11.169^{+0.014}_{-0.013}$
HS0705+6700	sdB	$0.53^{+0.25}_{-0.17}$	$0.226^{+0.017}_{-0.015}$	27^{+7}_{-6}	0.08 ± 0.006	0.8 ± 0.04	$-11.086^{+0.014}_{-0.013}$
HS0707+8225	sdB	$0.48^{+0.17}_{-0.13}$	$0.217^{+0.021}_{-0.018}$	25^{+7}_{-5}	$0.0421^{+0.0029}_{-0.006}$	0.59 ± 0.04	-11.243 ± 0.011
HS0740+3734	sdB	$0.42^{+0.14}_{-0.11}$	$0.251^{+0.018}_{-0.016}$	$13.2^{+2.7}_{-2.2}$	$0.0583^{+0.0023}_{-0.007}$	0.79 ± 0.04	$-11.051^{+0.008}_{-0.01}$
HS0741+3818	sdB	$0.48^{+0.18}_{-0.13}$	$0.242^{+0.023}_{-0.019}$	51^{+13}_{-10}	0.099 ± 0.006	0.62 ± 0.04	$-11.171^{+0.011}_{-0.01}$
HS0815+4243	sdOB	$0.72^{+0.27}_{-0.2}$	$0.139^{+0.016}_{-0.014}$	24^{+7}_{-5}	0.06 ± 0.007	0.49 ± 0.07	-11.51 ± 0.01
HS0941+4649	sdB	0.47 ± 0.08	$0.41^{+0.08}_{-0.07}$	180^{+80}_{-60}	$0.006^{+0.01}_{-0.007}$	0.03 ± 0.07	$-11.644^{+0.014}_{-0.012}$
HS0942+4608	binary	$0.1^{+0.06}_{-0.04}$	$0.135^{+0.012}_{-0.011}$	17^{+5}_{-4}	$0^{+0}_{-0.012}$	0.843 ± 0.023	-11.288 ± 0.025

HS1051+2933	sdOB	$0.29^{+0.12}_{-0.09}$	$0.093^{+0.012}_{-0.01}$	14^{+5}_{-4}	$0.024^{+0.004}_{-0.009}$	0.45 ± 0.1	$-11.722^{+0.01}_{-0.013}$
HS1106+6051	binary	$0.07^{+0.04}_{-0.021}$	$0.15^{+0.02}_{-0.017}$	27^{+9}_{-7}	$0.022^{+0.027}_{-0.022}$	0.533 ± 0.023	-11.45 ± 0.04
HS1236+4754	sdB	$0.4^{+0.16}_{-0.11}$	$0.187^{+0.019}_{-0.016}$	17^{+5}_{-4}	0.0075 ± 0.003	0.58 ± 0.05	-11.31 ± 0.011
HS1320+2622	sdB	$1.2^{+1.1}_{-0.5}$	$0.28^{+0.1}_{-0.06}$	50^{+40}_{-18}	0.044 ± 0.008	0.19 ± 0.09	$-11.61^{+0.011}_{-0.01}$
HS1511+6221	binary	$0.25^{+0.1}_{-0.08}$	$0.151^{+0.018}_{-0.016}$	130^{+50}_{-40}	$0.031^{+0.019}_{-0.02}$	0.57 ± 0.019	$-11.411^{+0.027}_{-0.029}$
HS1547+6312	sdB	$0.53^{+0.25}_{-0.17}$	$0.15^{+0.012}_{-0.011}$	22^{+6}_{-5}	$0.034^{+0.009}_{-0.015}$	0.852 ± 0.03	$-11.24^{+0.018}_{-0.017}$
HS1552+6333	sdB	$0.3^{+0.13}_{-0.09}$	$0.125^{+0.015}_{-0.012}$	21^{+6}_{-5}	$0.025^{+0.004}_{-0.005}$	0.5 ± 0.05	-11.548 ± 0.011
HS1556+6032	B?	$0.15^{+0.16}_{-0.07}$	$0.9^{+0.4}_{-0.21}$	18^{+18}_{-8}	$0^{+0.0018}_{-0}$	0.18 ± 0.04	$-11.141^{+0.015}_{-0.014}$
HS1612+6337	binary	$0.44^{+0.3}_{-0.17}$	$1.4^{+0.4}_{-0.25}$	$3.2^{+1.9}_{-1.1}$	$0^{+0.007}_{-0}$	0.27 ± 0.04	-10.77 ± 0.04
HS1612+7335	binary	$0.024^{+0.012}_{-0.008}$	$0.121^{+0.014}_{-0.012}$	15^{+5}_{-4}	$0^{+0}_{-0.007}$	0.663 ± 0.019	$-11.44^{+0.04}_{-0.03}$
HS1615+6341	binary	$0.06^{+0.04}_{-0.024}$	$0.2^{+0.04}_{-0.025}$	16^{+7}_{-5}	$0^{+0.009}_{-0}$	0.41 ± 0.04	$-11.43^{+0.028}_{-0.026}$
HS1641+4601	sdB	$0.4^{+0.13}_{-0.1}$	$0.149^{+0.01}_{-0.009}$	$16^{+4}_{-2.7}$	0.0102 ± 0.0025	0.89 ± 0.04	-11.223 ± 0.011
HS1717+6042	sdB	$0.43^{+0.14}_{-0.11}$	$0.177^{+0.011}_{-0.01}$	20 ± 4	$0.0272^{+0.0024}_{-0.0027}$	1.003 ± 0.028	$-11.098^{+0.011}_{-0.01}$
HS1736+8001	sdB	$0.15^{+0.06}_{-0.04}$	$0.233^{+0.023}_{-0.02}$	36^{+10}_{-8}	$0^{+0}_{-0.0012}$	0.6 ± 0.04	-11.199 ± 0.014
HS1739+5244	sdB	$0.57^{+0.21}_{-0.15}$	$0.174^{+0.018}_{-0.015}$	66^{+17}_{-14}	$0.041^{+0.005}_{-0.007}$	0.56 ± 0.04	$-11.359^{+0.009}_{-0.01}$
HS1741+2133	sdOB	$0.41^{+0.13}_{-0.1}$	$0.181^{+0.01}_{-0.009}$	65^{+12}_{-10}	0.142 ± 0.007	1.088 ± 0.026	-11.053 ± 0.01
HS1747+6924	sdB	$0.51^{+0.18}_{-0.13}$	$0.195^{+0.018}_{-0.015}$	19^{+5}_{-4}	$0.01^{+0.013}_{-0.011}$	0.65 ± 0.04	-11.246 ± 0.012
HS1747+8013	sdB	$0.5^{+0.4}_{-0.22}$	$0.2^{+0.04}_{-0.025}$	30^{+15}_{-10}	0.074 ± 0.006	0.37 ± 0.05	$-11.487^{+0.02}_{-0.021}$
HS1753+5342	binary	$0.032^{+0.015}_{-0.011}$	$0.096^{+0.013}_{-0.011}$	24^{+9}_{-6}	$0.02^{+0.04}_{-0.021}$	0.603 ± 0.023	-11.59 ± 0.04
HS1753+7025	binary	$0.053^{+0.023}_{-0.016}$	$0.178^{+0.024}_{-0.02}$	$11^{+4}_{-2.5}$	$0^{+0.006}_{-0}$	0.47 ± 0.04	-11.427 ± 0.024
HS1756+7056	sdB	$0.54^{+0.21}_{-0.15}$	$0.187^{+0.022}_{-0.018}$	22^{+7}_{-5}	$0.036^{+0.007}_{-0.014}$	0.51 ± 0.05	$-11.367^{+0.011}_{-0.017}$
HS1806+5024	sdOB	$0.46^{+0.25}_{-0.16}$	$0.17^{+0.04}_{-0.025}$	49^{+23}_{-14}	0.08 ± 0.007	0.3 ± 0.05	-11.623 ± 0.01
HS1813+7247	sdB	$0.25^{+0.11}_{-0.08}$	$0.215^{+0.021}_{-0.018}$	18^{+5}_{-4}	0.06 ± 0.009	0.61 ± 0.04	-11.226 ± 0.012
HS1824+5745	binary	$0.8^{+0.5}_{-0.29}$	$0.134^{+0.017}_{-0.014}$	20^{+7}_{-5}	$0.034^{+0.021}_{-0.017}$	0.48 ± 0.05	$-11.538^{+0.021}_{-0.017}$
HS1831+6432	sdOB	$0.38^{+0.12}_{-0.09}$	$0.11^{+0.008}_{-0.007}$	22^{+5}_{-4}	0.064 ± 0.007	0.86 ± 0.04	-11.369 ± 0.01
HS1831+7647	sdB	$0.44^{+0.13}_{-0.1}$	$0.226^{+0.014}_{-0.012}$	$12^{+2.2}_{-1.9}$	0.086 ± 0.004	0.942 ± 0.024	-11.017 ± 0.008
HS1832+7009	sdB	$0.22^{+0.07}_{-0.05}$	$0.136^{+0.007}_{-0.006}$	$9.6^{+1.6}_{-1.4}$	0.034 ± 0.0024	1.322 ± 0.029	-11.091 ± 0.01
HS1839+7951	sdB	$0.3^{+0.4}_{-0.15}$	$0.21^{+0.06}_{-0.04}$	12^{+11}_{-6}	0.037 ± 0.008	0.27 ± 0.07	$-11.576^{+0.03}_{-0.04}$
HS1842+6557	sdB	$2.2^{+2.2}_{-1.1}$	$0.138^{+0.014}_{-0.012}$	33^{+11}_{-8}	$0.049^{+0.006}_{-0.009}$	0.59 ± 0.04	$-11.432^{+0.016}_{-0.017}$
HS1843+6953	sdB	$0.43^{+0.16}_{-0.12}$	$0.164^{+0.016}_{-0.013}$	73^{+18}_{-15}	0.124 ± 0.009	0.62 ± 0.05	-11.338 ± 0.011
HS1844+5048	binary	$0.51^{+0.29}_{-0.18}$	$0.142^{+0.029}_{-0.021}$	190^{+100}_{-60}	0.112 ± 0.022	0.31 ± 0.04	$-11.697^{+0.024}_{-0.026}$
HS1846+8149	sdB	$0.43^{+0.13}_{-0.1}$	$0.192^{+0.012}_{-0.011}$	$14.9^{+2.7}_{-2.3}$	0.054 ± 0.005	0.954 ± 0.025	-11.084 ± 0.01
HS1858+5736	binary	$0.41^{+0.22}_{-0.14}$	$0.2^{+0.04}_{-0.028}$	50^{+22}_{-15}	$0.032^{+0.03}_{-0.029}$	0.387 ± 0.018	-11.46 ± 0.04
HS1859+6219	sdB	$0.3^{+0.11}_{-0.08}$	$0.197^{+0.017}_{-0.015}$	18^{+5}_{-4}	0.0429 ± 0.0028	0.67 ± 0.04	-11.226 ± 0.011
HS1917+7009	sdB	$0.42^{+0.14}_{-0.11}$	$0.212^{+0.016}_{-0.015}$	21^{+5}_{-4}	0.158 ± 0.011	0.761 ± 0.026	-11.137 ± 0.011
HS1926+6946	sdB	$0.14^{+0.08}_{-0.05}$	$0.22^{+0.021}_{-0.018}$	$11^{+4}_{-2.8}$	$0.156^{+0.008}_{-0.016}$	0.63 ± 0.04	$-11.202^{+0.008}_{-0.019}$
HS2005+7933	sdB	$0.28^{+0.12}_{-0.09}$	$0.233^{+0.024}_{-0.02}$	19^{+6}_{-4}	0.051 ± 0.004	0.56 ± 0.04	$-11.227^{+0.011}_{-0.012}$
HS2028+0107	sdOB	$0.35^{+0.17}_{-0.12}$	0.133 ± 0.008	23^{+5}_{-4}	0.2001 ± 0.0028	1 ± 0.05	$-11.224^{+0.012}_{-0.011}$
HS2029+0301	sdB	$0.3^{+0.1}_{-0.08}$	$0.118^{+0.008}_{-0.007}$	$11.4^{+2.2}_{-1.9}$	0.066 ± 0.004	0.93 ± 0.07	-11.307 ± 0.011
HS2033+0507	sdB	$1.1^{+0.8}_{-0.5}$	$0.34^{+0.08}_{-0.06}$	60^{+40}_{-18}	0.109 ± 0.004	0.27 ± 0.07	-11.382 ± 0.011
HS2035+0418	sdB	$0.54^{+0.19}_{-0.14}$	$0.231^{+0.019}_{-0.016}$	27^{+6}_{-5}	$0.077^{+0.004}_{-0.01}$	0.74 ± 0.05	$-11.114^{+0.011}_{-0.014}$
HS2100+1710	sdOB	$0.67^{+0.28}_{-0.2}$	$0.154^{+0.013}_{-0.011}$	30^{+7}_{-6}	0.085 ± 0.007	0.7 ± 0.04	$-11.312^{+0.012}_{-0.011}$
HS2100+1710 Run 2	sdOB	$0.59^{+0.19}_{-0.15}$	$0.151^{+0.013}_{-0.011}$	32^{+7}_{-6}	0.089 ± 0.007	0.7 ± 0.04	-11.319 ± 0.01
HS2126+8320	sdB	$0.19^{+0.09}_{-0.06}$	0.223 ± 0.012	14^{+4}_{-3}	0.071 ± 0.008	1.228 ± 0.023	$-10.908^{+0.014}_{-0.015}$
HS2126+8320 Run 2	sdB	$0.42^{+0.12}_{-0.1}$	$0.205^{+0.011}_{-0.01}$	21^{+4}_{-3}	0.101 ± 0.007	1.228 ± 0.023	-10.945 ± 0.011
HS2131+0349	B	$2^{+9}_{-1.4}$	$5^{+6}_{-1.7}$	500^{+2100}_{-400}	$0.0342^{+0.0023}_{-0.005}$	0.077 ± 0.029	$-10.78^{+0.008}_{-0.009}$
HS2143+8157	sdB	$0.24^{+0.1}_{-0.07}$	$0.214^{+0.021}_{-0.018}$	19^{+5}_{-4}	$0.109^{+0.005}_{-0.007}$	0.6 ± 0.04	$-11.235^{+0.012}_{-0.013}$

HS2149+0847	sdOB	$1.6^{+1.2}_{-0.7}$	$0.18^{+0.05}_{-0.03}$	60^{+40}_{-18}	$0.046^{+0.005}_{-0.02}$	0.27 ± 0.1	$-11.647^{+0.012}_{-0.021}$
HS2149+1428	sdB	$0.7^{+0.4}_{-0.24}$	$0.2^{+0.015}_{-0.014}$	63^{+16}_{-13}	$0.1059^{+0.0023}_{-0.0025}$	0.78 ± 0.04	$-11.153^{+0.013}_{-0.012}$
HS2151+0214	sdB	$0.29^{+0.11}_{-0.08}$	$0.118^{+0.011}_{-0.01}$	$11.6^{+2.8}_{-2.2}$	$0.07^{+0.004}_{-0.011}$	0.62 ± 0.11	$-11.481^{+0.01}_{-0.014}$
HS2151+0857	binary	$0.7^{+0.6}_{-0.3}$	$0.144^{+0.024}_{-0.019}$	26^{+11}_{-8}	0.062 ± 0.016	0.37 ± 0.07	-11.614 ± 0.02
HS2156+2215	sdOB	$0.35^{+0.14}_{-0.1}$	$0.182^{+0.02}_{-0.017}$	47^{+13}_{-10}	$0.079^{+0.007}_{-0.016}$	0.54 ± 0.06	$-11.354^{+0.008}_{-0.017}$
HS2156+2517	sdB	$0.51^{+0.16}_{-0.12}$	$0.1^{+0.006}_{-0.005}$	$16.3^{+2.9}_{-2.5}$	$0.0599^{+0.0028}_{-0.005}$	1.05 ± 0.06	$-11.322^{+0.009}_{-0.01}$
HS2158+2137	sdB	$0.39^{+0.11}_{-0.09}$	0.119 ± 0.005	$12.7^{+2}_{-1.7}$	0.094 ± 0.003	1.6 ± 0.05	-11.064 ± 0.01
HS2201+2610	sdB	$0.69^{+0.22}_{-0.17}$	$0.226^{+0.017}_{-0.015}$	31^{+7}_{-6}	$0.0541^{+0.0025}_{-0.0029}$	0.76 ± 0.04	$-11.114^{+0.011}_{-0.01}$
HS2206+2847	sdB	$0.62^{+0.2}_{-0.15}$	$0.158^{+0.012}_{-0.011}$	22^{+5}_{-4}	0.096 ± 0.004	0.77 ± 0.04	-11.262 ± 0.01
HS2208+2718	sdB	$0.53^{+0.18}_{-0.14}$	$0.195^{+0.017}_{-0.015}$	24^{+6}_{-5}	$0.076^{+0.004}_{-0.007}$	0.65 ± 0.05	$-11.240^{+0.01}_{-0.011}$
HS2209+2840	sdB	$0.44^{+0.16}_{-0.12}$	$0.139^{+0.013}_{-0.011}$	$14^{+4}_{-2.6}$	$0.063^{+0.004}_{-0.012}$	0.66 ± 0.05	$-11.385^{+0.01}_{-0.015}$
HS2213+1336	sdB	$0.41^{+0.22}_{-0.14}$	$0.41^{+0.08}_{-0.06}$	24^{+11}_{-7}	$0^{+0}_{-0.0015}$	0.33 ± 0.05	-11.21 ± 0.014
HS2216+1833	binary	$0.07^{+0.04}_{-0.024}$	$0.139^{+0.019}_{-0.017}$	20^{+7}_{-5}	0.08 ± 0.06	1.23 ± 0.05	-11.11 ± 0.06
HS2218+0201	sdB	$0.37^{+0.11}_{-0.09}$	$0.231^{+0.013}_{-0.012}$	$18^{+4}_{-2.7}$	$0.0941^{+0.0028}_{-0.0029}$	1.09 ± 0.04	$-10.943^{+0.009}_{-0.01}$
HS2224+2618	sdB	$0.44^{+0.15}_{-0.11}$	0.46 ± 0.04	35^{+8}_{-7}	$0^{+0}_{-0.0007}$	0.73 ± 0.04	-10.82 ± 0.011
HS2225+2220	sdB	$0.42^{+0.15}_{-0.11}$	$0.129^{+0.012}_{-0.011}$	$13^{+4}_{-2.6}$	$0.041^{+0.011}_{-0.023}$	0.64 ± 0.07	$-11.423^{+0.01}_{-0.025}$
HS2229+0910	sdOB	$0.79^{+0.28}_{-0.21}$	$0.116^{+0.007}_{-0.006}$	25^{+5}_{-4}	0.114 ± 0.006	1.05 ± 0.06	$-11.263^{+0.01}_{-0.009}$
HS2229+2628	HBB	$0.6^{+0.5}_{-0.22}$	$0.73^{+0.18}_{-0.12}$	70^{+50}_{-24}	$0.078^{+0.004}_{-0.008}$	0.26 ± 0.04	$-11.069^{+0.009}_{-0.011}$
HS2231+2441	sdB	$0.48^{+0.14}_{-0.11}$	$0.19^{+0.011}_{-0.01}$	20^{+4}_{-3}	$0.047^{+0.004}_{-0.005}$	1.1 ± 0.05	-11.024 ± 0.011
HS2233+1418	sdOB	$0.82^{+0.3}_{-0.22}$	$0.199^{+0.013}_{-0.012}$	83^{+17}_{-14}	0.076 ± 0.004	0.89 ± 0.09	-11.1 ± 0.01
HS2233+2332	sdB	$0.42^{+0.13}_{-0.1}$	$0.205^{+0.013}_{-0.012}$	19^{+4}_{-3}	$0.0354^{+0.0024}_{-0.0029}$	0.95 ± 0.05	-11.058 ± 0.01
HS2233+2332 Run 2	sdB	$0.31^{+0.1}_{-0.08}$	$0.214^{+0.013}_{-0.012}$	$16.1^{+3}_{-2.5}$	0.0222 ± 0.0024	0.95 ± 0.05	$-11.038^{+0.009}_{-0.01}$
HS2240+0136	sdB	$0.42^{+0.12}_{-0.1}$	0.116 ± 0.005	$11.1^{+1.8}_{-1.6}$	0.078 ± 0.005	1.53 ± 0.04	$-11.099^{+0.011}_{-0.01}$
HS2240+1031	sdOB	$0.31^{+0.1}_{-0.08}$	$0.143^{+0.01}_{-0.009}$	26^{+6}_{-5}	$0.067^{+0.004}_{-0.005}$	0.83 ± 0.05	$-11.271^{+0.01}_{-0.011}$
HS2242+3206	sdB	$0.55^{+0.16}_{-0.12}$	$0.165^{+0.008}_{-0.007}$	$16.4^{+2.6}_{-2.3}$	$0.0912^{+0.002}_{-0.004}$	1.45 ± 0.04	$-10.967^{+0.011}_{-0.01}$
HS2246+0158	sdB	$0.33^{+0.13}_{-0.09}$	$0.119^{+0.009}_{-0.008}$	18 ± 4	0.095 ± 0.005	0.77 ± 0.07	-11.383 ± 0.011
HS2333+3927	sdOB	$0.76^{+0.24}_{-0.18}$	$0.163^{+0.011}_{-0.01}$	58^{+12}_{-10}	$0^{+0}_{-0.0017}$	0.87 ± 0.04	$-11.198^{+0.011}_{-0.01}$
HS2333+3927 Run 2	sdOB	$0.57^{+0.18}_{-0.14}$	$0.154^{+0.011}_{-0.01}$	72^{+14}_{-12}	$0^{+0}_{-0.0017}$	0.87 ± 0.04	-11.221 ± 0.01

Table 4: Table of temperature and stellar parameters for the binaries in this sample. Listed are the temperature, radius and luminosity of the subdwarf (sd) and its companion (comp) as well as the colour excess E(44-55). HS1612+6337 may be a binary of two main-sequence stars. HS0136+0605 is an eclipsing binary system (Papageorgiou et al., 2018) but no composite SED could be fitted.

Name	$T_{\rm eff,sd}$ [K]	$R_{\rm sd}$ [$R_\odot$]	$L_{\rm sd}$ [$L_\odot$]	$T_{\rm eff,comp}$ [K]	$R_{\rm comp}$ [$R_\odot$]	$L_{\rm comp}$ [$L_\odot$]	E(44-55) [mag]
HS0016+0044	27300 ± 1100	$0.215^{+0.021}_{-0.018}$	23^{+7}_{-5}	4810^{+50}_{-100}	$0.64^{+0.07}_{-0.06}$	$0.19^{+0.05}_{-0.04}$	$0^{+0.009}_{-0}$
HS0028+4408	34500 ± 1400	$0.23^{+0.07}_{-0.05}$	70^{+50}_{-23}	5710^{+240}_{-100}	$2^{+0.6}_{-0.5}$	$3.9^{+2.8}_{-1.7}$	$0.02^{+0.09}_{-0.02}$
HS0127+3146	37400 ± 1200	$0.28^{+0.05}_{-0.04}$	140^{+60}_{-40}	6160^{+150}_{-400}	$1.13^{+0.23}_{-0.19}$	$1.6^{+0.8}_{-0.6}$	$0^{+0.07}_{-0.004}$
HS0136+0605	19700 ± 900	$0.053^{+0.006}_{-0.005}$	$0.37^{+0.12}_{-0.09}$	8000^{+260}_{-90}	$1.56^{+0.16}_{-0.14}$	$9.3^{+2.3}_{-1.7}$	$0.14^{+0.04}_{-0.011}$
HS0215+0852	43000 ± 5000	$0.119^{+0.015}_{-0.013}$	45^{+24}_{-17}	6470^{+60}_{-70}	$1.15^{+0.15}_{-0.13}$	$2.1^{+0.6}_{-0.5}$	$0^{+0}_{-0.015}$
HS0232+3155	35900 ± 1200	$0.128^{+0.009}_{-0.008}$	24^{+5}_{-4}	4130^{+270}_{-240}	$0.48^{+0.05}_{-0.04}$	$0.06^{+0.021}_{-0.016}$	$0.167^{+0.012}_{-0.014}$
HS0252+1025	42800 ± 1400	$0.161^{+0.022}_{-0.024}$	78^{+26}_{-22}	5680^{+240}_{-400}	$0.76^{+0.18}_{-0.15}$	$0.5^{+0.4}_{-0.2}$	$0.24^{+0.06}_{-0.07}$
HS0446+1344	50300 ± 1600	$0.189^{+0.021}_{-0.019}$	200^{+60}_{-50}	6600^{+180}_{-220}	$0.85^{+0.13}_{-0.12}$	$1.2^{+0.5}_{-0.4}$	$0.286^{+0.03}_{-0.04}$
HS0656+6117	30900 ± 2200	$0.154^{+0.021}_{-0.017}$	20^{+9}_{-6}	5010 ± 70	$0.99^{+0.14}_{-0.12}$	$0.55^{+0.17}_{-0.12}$	$0.099^{+0.014}_{-0.015}$
HS0942+4608	32000 ± 1500	$0.135^{+0.012}_{-0.011}$	17^{+5}_{-4}	5540 ± 50	$1.26^{+0.12}_{-0.1}$	$1.34^{+0.26}_{-0.21}$	$0^{+0}_{-0.012}$
HS1106+6051	34000 ± 1200	$0.15^{+0.02}_{-0.017}$	27^{+9}_{-7}	6390^{+110}_{-120}	$1.17^{+0.18}_{-0.16}$	$2.1^{+0.7}_{-0.6}$	$0.022^{+0.027}_{-0.022}$
HS1511+6221	50600 ± 1900	$0.151^{+0.018}_{-0.016}$	130^{+50}_{-40}	6400^{+110}_{-100}	$1.17^{+0.16}_{-0.14}$	$2.1^{+0.7}_{-0.5}$	$0.031^{+0.019}_{-0.02}$
HS1612+6337	6550 ± 200	$1.4^{+0.4}_{-0.25}$	$3.2^{+1.9}_{-1.1}$	3700^{+700}_{-900}	$1.1^{+0.5}_{-0.4}$	$0.2^{+0.4}_{-0.15}$	$0^{+0.007}_{-0}$
HS1612+7335	32600 ± 1400	$0.121^{+0.014}_{-0.012}$	15^{+5}_{-4}	6900^{+110}_{-140}	$1.08^{+0.13}_{-0.12}$	$2.4^{+0.7}_{-0.5}$	$0^{+0}_{-0.007}$
HS1615+6341	25800 ± 1100	$0.2^{+0.04}_{-0.025}$	16^{+7}_{-5}	4780 ± 130	$1.27^{+0.21}_{-0.17}$	$0.75^{+0.28}_{-0.2}$	$0^{+0.009}_{-0}$
HS1753+5342	41400 ± 1700	$0.096^{+0.013}_{-0.011}$	24^{+9}_{-6}	6040^{+110}_{-100}	$0.9^{+0.15}_{-0.13}$	$1^{+0.4}_{-0.26}$	$0.02^{+0.04}_{-0.021}$
HS1753+7025	24600 ± 800	$0.178^{+0.024}_{-0.02}$	$11^{+4}_{-2.5}$	6300 ± 100	$0.99^{+0.14}_{-0.11}$	$1.4^{+0.5}_{-0.3}$	$0^{+0.006}_{-0}$
HS1824+5745	33500 ± 1400	$0.134^{+0.017}_{-0.014}$	20^{+7}_{-5}	4310^{+170}_{-260}	$0.65^{+0.09}_{-0.08}$	$0.13^{+0.05}_{-0.04}$	$0.034^{+0.021}_{-0.017}$
HS1844+5048	56900 ± 2200	$0.142^{+0.029}_{-0.021}$	190^{+100}_{-60}	5340^{+290}_{-280}	$0.84^{+0.18}_{-0.14}$	$0.52^{+0.29}_{-0.18}$	0.112 ± 0.022
HS1858+5736	34500 ± 1300	$0.2^{+0.04}_{-0.028}$	50^{+22}_{-15}	6760^{+130}_{-120}	$1.47^{+0.3}_{-0.25}$	$4.1^{+1.9}_{-1.3}$	$0.032^{+0.03}_{-0.029}$
HS2151+0857	34200 ± 1700	$0.144^{+0.024}_{-0.019}$	26^{+11}_{-8}	4230^{+220}_{-270}	$0.75^{+0.13}_{-0.11}$	$0.16^{+0.08}_{-0.06}$	0.062 ± 0.016
HS2216+1833	32600 ± 1300	$0.139^{+0.019}_{-0.017}$	20^{+7}_{-5}	5630 ± 90	$0.89^{+0.18}_{-0.16}$	$0.7^{+0.4}_{-0.23}$	0.08 ± 0.06

Acknowledgements

I would like to thank Uli Heber for showing me the field of stellar astrophysics and giving me the opportunity to study in this part of physics. I would also like to thank him for the advise and discussions during the making of this thesis. The next thank you is dedicated to Matti Dorsch, Stephan Geier and Aakash Bhat for the weekly meetings in which I was able to learn a lot about current research in hot subdwarfs. I also want to thank Andreas Irrgang for providing the analysis scripts and Heinz Edelmann for providing the spectra for this thesis. Last but not least I want to thank my fellow students Sebastian Weich, Anna Gebhardt and Maximilian Halenke for the discussions.

Eidesstattliche Erklärung

Ich erkläre hiermit, dass ich die vorliegende Arbeit selbständig verfasst, andere als die angegebenen Quellen/Hilfsmittel nicht benutzt, und die den benutzten Quellen wörtlich und inhaltlich entnommenen Stellen als solche kenntlich gemacht habe.

Erlangen, 10.4.2024
Ort, Datum

Lennard Kufleitner